

## Young Clusters in the Nuclear Starburst of M 83<sup>1</sup>

Jason Harris

*Space Telescope Science Institute*

*3700 San Martin Dr., Baltimore, MD, 21218*

*E-Mail: jharris@stsci.edu*

Daniela Calzetti

*Space Telescope Science Institute*

*3700 San Martin Dr., Baltimore, MD, 21218*

*E-Mail: calzetti@stsci.edu*

John S. Gallagher III

*Dept. of Astronomy, University of Wisconsin-Madison*

*475 North Charter Street, Madison, WI 53706*

*E-Mail: jsg@astro.wisc.edu*

Christopher J. Conselice and Denise A. Smith<sup>2</sup>

*Space Telescope Science Institute*

*3700 San Martin Dr., Baltimore, MD, 21218*

*consel@stsci.edu, dsmith@stsci.edu*

### ABSTRACT

We present a photometric catalog of 45 massive star clusters in the nuclear starburst of M 83 (NGC 5236), observed with the Hubble Space Telescope WFPC2, in both broad-band (F300W, F547M, and F814W) and narrow-band (F656N and F487N) filters. By comparing the photometry to theoretical population synthesis models, we estimate the age and mass of each cluster. We find that over 75% of the star clusters more massive

---

<sup>1</sup>Based on observations obtained with the NASA/ESA *Hubble Space Telescope* at the Space Telescope Science Institute, which is operated by the Association of Universities for Research in Astronomy, Inc., under NASA contract NAS5-26555.

<sup>2</sup>Computer Sciences Corporation

than  $2 \times 10^4 M_{\odot}$  in the central 300 pc of M 83 are less than 10 Myr old. Among the clusters younger than 10 Myr and more massive than  $5 \times 10^3 M_{\odot}$ , 70% are between 5 and 7 Myr old. We list an additional 330 clusters that are detected in our F300W images, but not in the shallower F547M and F814W images. The clusters are distributed throughout a semicircular annulus that identifies the active region in the galaxy core, between 50 and 130 pc from the optical center of M 83. Clusters younger than 5 Myr are preferentially found along the perimeter of the semicircular annulus. We suggest that the 5–7 Myr population has evacuated much of the interstellar material from the active ringlet region, and that star formation is continuing along the edges of the region.

*Subject headings:* galaxies: starburst — galaxies: star clusters — galaxies: individual: NGC 5236

## 1. Introduction

A significant fraction of star formation in the universe may have occurred in high-intensity bursts. In the local universe, starburst galaxies and spiral galaxies contribute roughly equally to the total number of massive stars, despite the fact that spirals are much more numerous (Heckman et al. 1998). At intermediate redshifts, the faint blue galaxy population may be composed of dwarf galaxies undergoing intense, rapidly-evolving starbursts (*e.g.*, Colless et al. 1994; Phillipps & Driver 1995). Finally, the Lyman-break galaxies at  $z \sim 3$  show evidence for intense star formation (Steidel et al. 1996, 1999). Because starbursts are a significant source of massive stars, from the local universe out to  $z \sim 3$ , they are a fundamental part of understanding the star formation history of galaxies, and the chemical enrichment of the universe.

Local starbursts make excellent laboratories for unraveling the starburst mechanism, because their proximity affords superb spatial resolution. Local starbursts are quite similar to high-redshift ( $z \gtrsim 2.5$ ) active galaxies in star formation rate (Meurer et al. 1997; Kennicutt et al. 1998), UV colors (Meurer et al. 1997, 1999; Adelberger & Steidel 2000), and spectral morphology (Steidel et al. 1996; Lowenthal et al. 1997; Pettini et al. 2000), although the high-redshift galaxies tend to have higher surface brightness than local starbursts (Weedman et al. 1998). Because of the many similarities, detailed photometric and spectroscopic studies of local starbursts can constrain the processes which govern star formation in active galaxies, and provide a foundation for understanding the high-redshift objects. In particular, we wish to address the following questions: (1) Are starburst properties determined by global properties of the host galaxy? (2) What are the mechanisms that sustain starbursts? (3) How long do starbursts last? (4) Does star formation propagate in starburst galaxies? What is the propagation mechanism? (5) Do most stars form in clusters (which then dissolve to form the field population), or are there distinct modes of star formation for forming clusters and field stars?

We are undertaking a study of local starburst galaxies to examine these questions. The subject

of this paper is our photometric study of M 83 (NGC 5236), with an emphasis on its star clusters. M 83 is a nearby (3.7 Mpc, de Vaucouleurs 1979) starburst galaxy. It has a close dynamical companion in NGC 5253 (Rogstad et al. 1974); these two very different galaxies contain similarly intense nuclear starbursts (Calzetti et al. 1997, 1999; Tremonti et al. 2001). The central starburst in M 83 spans 20 arcsec ( $\sim 360$  pc at 3.7 Mpc), and presents a relatively complex morphology (see Gallais et al. 1991; Elmegreen et al. 1998). In contrast to the centrally-concentrated starburst of NGC 5253, the optically-detected starburst in M 83 is contained in a semi-circular annulus between 3" and 7" (54 pc and 126 pc at 3.7 Mpc distance) from M 83's optical center (Thatte et al. 2000). This "active ringlet" region contains almost 400 star clusters brighter than  $m_{F300W} = 18$  mag, and 45 of these are bright enough to be detected in the shallower F547M and F814W images.

The nuclear region of M83 has several unusual properties, so we are not surprised to find that it hosts a complex starburst region. Located within the main bar of M83, the center of the galaxy appears to contain a well-defined nuclear subsystem. A bright optical nucleus is offset from the center of the outer isophotes opposite to the starburst ringlet (Gallais et al. 1991), and a nuclear bar may separate these two objects (Elmegreen et al. 1998). Dense molecular gas is present and generally concentrated to the north of the starburst ringlet (Israel & Baas 2001), perhaps a result of material collecting around an inner Lindblad resonance, as suggested by Gallais et al.. Near infrared spectroscopy by Puxley et al. (1997) confirms that young populations are offset from the optically visible nucleus, corresponding to the optical starburst ringlet. Thatte et al. (2000) find that the optically visible nucleus, as well as a second obscured nucleus at the center of symmetry, are dominated by older red giant stars.

The picture emerging from these observations is of a complicated situation, where the absence of axisymmetry is playing a role in shaping ongoing events. The probable double nucleus suggests that another galaxy merged with M83 in the past; its nuclear starburst was not necessarily triggered only by the interaction with NGC 5253. Since orbital time scales are short,  $<10^7$  yr within the starburst ringlet, the asymmetric distribution of star forming activity evidently survived for several orbits to explain the observed variations in cluster ages (see Section 5). Furthermore, given the small distances involved and the near rigid body inner rotation curve found by Thatte et al., propagation of star formation even at the relatively low speed of  $10 \text{ km s}^{-1}$  suffices to produce a starburst on the scale of the ringlet in  $\sim 10$  Myr. Possibly, the starburst is a transitory flare-up of circum-nuclear star formation, in which molecular cloud complexes such as those now present around the nucleus are rapidly disrupted, rather than a long term event. The age distribution of star clusters can shed light on this issue.

The paper is organized as follows: we present the observations and data reduction in Section 2; photometry of the stellar clusters and dust corrections are described in Sections 3 and 4, respectively; age and mass determinations of the clusters are made in Section 5, while the properties of the diffuse population in the starburst site are described in Section 6. We discuss the results of our study in Section 7, and summarize the paper in Section 8.

## 2. Observations and Data Reduction

M 83 was observed with the Hubble Space Telescope (HST) Wide Field and Planetary Camera 2 (WFPC2), in the broad-band filters F300W, F547M and F814W and in the narrow-band filters F487N and F656N, in two separate visits one week apart during April-May, 2000 (see Figure 1). The log of the exposures, together with the exposure times and the characteristics of the filters are listed in Table 1. Images of the galaxy in the F502N and F673N filters were also obtained during the same visits and will be discussed in an accompanying paper (Calzetti et al. 2001). The central starburst of the galaxy is about  $20''$  in diameter and is perfectly matched with the PC1 chip ( $36'' \times 36''$ ), on which it was centered. The telescope orientation was about  $+74.3$  degrees off North, and the rotation between the images obtained in the two visits is small.

In each of the filters, two or three separate exposures were obtained to aid in cosmic ray rejection. The F300W filter probes the galaxy UV emission; the F814W filter is the WFPC2 equivalent I band; the F547M filter is used here as a V-band equivalent, and was preferred to the wider F555W filter because its bandpass excludes the strong [OIII](5007 Å) nebular emission from the galaxy. The recession velocity of M83 is sufficiently small ( $516 \text{ km s}^{-1}$ ) that the two narrow band filters probe the hydrogen recombination emission lines  $H\beta$ (4861 Å) and  $H\alpha$ (6563 Å), respectively. The F656N filter is narrow enough to exclude the redshifted [NII](6584 Å) emission line; however, the [NII](6548 Å) emission line falls within the filter’s bandpass and represents about 15% of the  $H\alpha$  line flux in the filter, as inferred from spectroscopic data (Storchi-Bergmann et al. 1994).

The data were reduced by the STScI calibration pipeline, which includes flagging of bad pixels, A/D conversion, bias and dark current subtraction, and flatfielding. Hot pixels were removed using the STSDAS routine WARMPIX, which uses hot pixel information from dark frames obtained around the time of the science observations to perform the correction. The reduced images were registered to a common position using linear shifts and small rotations; cosmic ray rejection and co-addition were performed using the STSDAS routine CRREJ (Williams et al. 1996), with a rejection threshold of  $4 \sigma$  for the cosmic rays and  $2.4 \sigma$  for the adjacent pixels. The absolute photometric calibration of the images is obtained from the zero-points listed in HST Data Handbook (Voit 1997), and have about 2%–5% accuracy in the medium and broad-band filters (Casertano 1997). The effect of contaminant buildup onto the WFPC2 window is negligible at optical wavelengths, and was also negligible (less than 1%) in the F300W filter in this instance, because the observations were obtained 7 days after decontamination. A correction of 2% to the total counts was applied to the narrow-band images to correct for the Charge Transfer Efficiency (CTE) problem of WFPC2 (Stetson 1998; Whitmore et al. 1999).

Images of the nebular emission in  $H\alpha + [NII](6548 \text{ Å})$  and in  $H\beta$  were constructed by subtracting the stellar continuum from the narrow band images. The image of the stellar continuum underlying each of the lines was estimated from one of the broadband images (F547M and F814W for F487N and F656N, respectively). We used the optical spectrum of Storchi-Bergmann et al. (1995) as a

reference for determining a constant normalization factor applied to the broadband images. Because of the galaxy’s recession velocity, the  $H\alpha$  line falls close to the F656N red wing and a correction of about 25% was necessary to recover the full line flux; the line flux was then corrected for the average value of the  $[NII](6548 \text{ \AA})$  contribution (Storchi-Bergmann et al. 1994), to obtain a final  $H\alpha$  image. A 2% correction for the filter transmission curve was applied to the  $H\beta$  image. The effect of the underlying stellar absorption is larger for the weak  $H\beta$  emission than for  $H\alpha$ . Using red stellar objects to scale the continuum image to the narrow-band image can introduce a bias in the continuum subtraction of the blue stars, depending on the red stellar population. For example, an F/G type population has a relatively high  $H\beta$  absorption equivalent width, which would lead to undersubtraction of the OB stars continuum; on the other hand, a K-type population with small Balmer equivalent widths (EWs) would lead to over-subtraction of the blue stellar continuum. In this case, a default correction of  $2 \text{ \AA}$  for the underlying stellar absorption was applied to the  $H\beta$  image, but individual cases will be evaluated independently in the following analysis. The continuum-subtraction and calibration of the emission line images were cross-checked against the spectroscopic data of Storchi-Bergmann et al. (1995). Fluxes were extracted from the images using the same aperture size and orientation of the spectrum ( $10'' \times 20''$ , with the largest size along the E-W direction). The aperture was centered at the peak of the optical emission in the images (about the center of the PC-1 chip). The flux densities as measured from the images are only a few percent different than the values obtained from the spectrum convolved with the WFPC2 filters bandpasses, confirming the accuracy of our extraction.

### 3. Star Cluster Photometry

Crowding in the starburst region of M 83 complicates the identification of star clusters, and the accurate extraction of their photometry. We opted for profile-fitting photometry, rather than aperture photometry, as the former allows us to disentangle partially overlapping clusters and derive accurate total fluxes in each band. In addition, profile fitting allows one to empirically check the accuracy of the local background determination (a major source of uncertainty in aperture photometry). If the background of an object is poorly determined, it will leave a circular pixel-value discontinuity in the residual object-subtracted image. We can then iterate the fit until the residual image is smooth.

Profile fitting is typically applied to unresolved objects, which are well-described by a single Point-Spread Function (PSF) across the entire image or field. The star clusters in M 83 are resolved in the high angular resolution HST images; in the case of resolved objects, PSF fitting can only be applied if the object profiles are uniform. However, the clusters in our sample have profiles that vary in significant and complex ways. The half-light radius varies, and some of the clusters have a sharp core feature superimposed on a broader profile. As an added complication, the core feature can have a small, random offset from the centroid of the underlying profile. To circumvent these problems, we convolve each of the images with a small Gaussian kernel ( $\sigma = 2$  pixels), in order to

get sufficiently uniform cluster profiles that can be well-fit by a single PSF model. The Gaussian kernel is large enough to homogenize the cluster profiles, and small enough that blending of clusters is not a concern (2 pixels corresponds to less than 2 pc at the distance of M 83).

We use DAOPHOT (Stetson 1987) to perform iterative profile fitting on the Gaussian-convolved images. Objects are detected using DAOFIND, with a  $10\sigma$  detection threshold. We obtain preliminary photometry with PHOT, using a 3-pixel aperture. Around 12 PSF objects are selected with PSTSELECT, and the best-fit profile is determined using PSF with a PSF radius of 11 pixels, and a fitting radius of 3 pixels. We allow PSF to use all available functions in modeling the profiles (Gaussian, Lorentz, Moffat, and Penny functions are attempted). The PSF is then used to subtract objects from the image using SUBSTAR. We examine the subtracted image for undetected objects near the PSF objects (which are added to the list of objects to be subtracted), and for poorly-fit PSF objects (which are removed from the list of PSF objects). We then run PSF again on an image in which objects near the PSF objects have been subtracted. The images require between three and six such iterations to obtain cleanly subtracted images (see Figure 2). When we have obtained a satisfactory PSF model, we use ALLSTAR to obtain profile photometry of all detected objects. Since the magnitudes returned by the ALLSTAR routine are normalized to a 3-pixel aperture, we need to determine the aperture correction for each image to obtain total magnitudes.

Aperture corrections are difficult to measure directly in these images, because of the crowding of objects and the non-uniform background light. We therefore determine the aperture corrections using artificial objects, added to the relatively empty image regions outside the active ringlet region. Artificial objects are added to each image using the DAOPHOT ADDSTAR routine, which constructs the objects from the image’s best-fit PSF. The artificial objects are placed in a uniform grid, separated by 26 pixels in each direction. This ensures that the PSFs do not overlap, since the PSF radius used is 11 pixels. Once the artificial objects are added, we select objects in isolated regions of the frame, and perform both ALLSTAR photometry and concentric aperture photometry on the isolated artificial objects. The aperture correction is defined as the difference between the 13-pixel radius aperture magnitude and the ALLSTAR magnitude. Figure 3 shows a histogram of the aperture corrections from a series of F547M frames with artificial objects added. We fit a Gaussian to the peak to determine both the mean aperture correction and its contribution to the photometric errors. We find that the scatter in the aperture correction dominates the photometric error in all images (note that because the distribution of aperture corrections has non-Gaussian tails, these photometric errors may be somewhat underestimated).

We also use artificial-object tests to determine the completeness limits in each image. In this case, we add objects to the populated regions of the image, so that the proper background levels and crowding environments are sampled. We estimate that the photometry is 90% complete to 19.0 mag, 19.1 mag, and 19.6 mag, and 50% complete to 19.8 mag, 20.3 mag, and 20.4 mag for the F300W, F547M, and F814W images, respectively. Because of the finite number of artificial objects used, the uncertainty in these completeness limits is approximately 0.2 mag. We convert these photometric completeness limits to an age-dependent mass limit in Section 7.

These artificial object tests also allow us to test the accuracy of profile-fitting photometry, relative to aperture photometry. We find that the profile-fitting photometry recovers the input artificial magnitudes as accurately as does aperture photometry. In fact, profile-fitting is somewhat more accurate in highly crowded regions, as we expected.

We produce a photometric catalog of star clusters by positionally matching detected objects in the F300W, F547M and F814W images. Only objects which could be matched in all three images are included, and the final catalog contains 45 star clusters (for a discussion of potential selection effects, see section 7). The astrometry and broad/medium band photometry of the clusters in our sample are presented in Table 2.

Because the exposure time of the F300W image was twice as long as either the F547M or F814W images (Table 1), there are over 300 faint clusters detected in F300W, which were not detected in either F547M or F814W. 64 of these clusters were detected in F547M, so we have at least the  $(m_{F300W} - m_{F547M})$  color for these objects. We can constrain the age of these clusters by examining the Starburst99 model (see Figure 6): all model points with  $(m_{F300W} - m_{F547M}) \lesssim -1.2$  are younger than 10 Myr. We therefore estimate that at least 42 of the 64 clusters detected in both F300W and F547M are younger than 10 Myr. We also attempted to constrain the ages of the remaining F300W-detected clusters, by finding upper limits on their  $(m_{F300W} - m_{F547M})$  colors. However, the color limits are widely and uniformly distributed, so no significant constraint on the ages was possible. We present the astrometry and photometry of these F300W-detected objects in Table 3.

We perform a similar profile-fitting photometry procedure on the narrow-band F656N ( $H\alpha$ ) image (see Figure 4, left panel). Once the F656N magnitudes are determined, we calculate the  $H\alpha$  flux by using the same procedure described in Section 2 for the F656N image as a whole. A one-to-one match between optically-detected clusters and F656N peaks cannot always be found in our images, because the ionized gas associated with a cluster is not necessarily spatially coincident with the cluster. For example, evolving clusters can generate gas outflows that clear the cluster’s region of gas and dust, as observed in the 30 Doradus nebula by Scowen et al. (1998) and Walborn et al. (1999). Therefore, we choose to associate each peak detected in F656N with the nearest cluster, as long as the cluster lies within a maximum search radius. In this way, a single cluster can accumulate the flux from several nearby F656N peaks. Because we are attempting to associate ionized gas with its photoionizing source, we include all clusters detected in F300W in this matching, regardless of whether they are in our final photometric catalog. In practice, it is difficult to choose an appropriate size for the maximum search radius. We present two limiting cases: a smaller radius of 5 pc, and a larger 12 pc radius. These two strategies yield identical F656N fluxes for all but three of the 45 bright clusters in our sample. There is one bright cluster (# 28) for which no matching F656N peak could be found. We place an upper limit on the F656N flux associated with this object by measuring the flux in an 11-pixel aperture centered on the cluster in the peak-subtracted F656N image. The F656N flux is converted to an  $H\alpha$  flux using the procedure already described. We derive the equivalent widths of the  $H\alpha$  emission ( $EW(H\alpha)$ ) for each cluster from the  $H\alpha$  flux

measurement, using the F814W flux associated with the cluster to estimate the stellar continuum. In Section 5, we use the  $\text{EW}(H\alpha)$  values to help constrain the cluster ages. The  $\text{EW}(H\alpha)$  values are presented in Table 2.

#### 4. Dust Attenuation

We use the  $H\alpha$  and  $H\beta$  images to estimate dust extinction corrections to the photometry. The distribution of interstellar dust is very complicated in the center of M 83, because of the presence of an opaque dust lane (Telesco et al. 1993) and inhomogeneous dust and light distributions. We measure the ratio  $R = F(H\alpha)/F(H\beta)$  at each cluster location (see Figure 4, right panel), and determine the  $E(B - V)$  color excess using the standard formula for foreground dust, appropriate for line emission in starburst galaxies (Calzetti 1997), and adopting an intrinsic ratio  $R_{int}=2.75$  (Osterbrock 1989). In Figure 5, we show the distribution of inferred  $E(B-V)$  values for all pixels with  $R > 2.75$ . The significant width of the distribution and its tail to high  $E(B-V)$  values underscore the importance of determining an independent reddening correction for each cluster.

Once the  $E(B - V)$  color excess is determined for each cluster, we use a two-component extinction model to deredden the photometry. The extinction model consists of a foreground Milky Way component ( $E(B - V)_{MW} = 0.06$ , Schlegel et al. 1998) and an internal component that follows the starburst extinction curve (Calzetti et al. 1994, 2000):

$$A_{300} = 3.07 \times (E(B - V) - 0.06) + 5.59 \times 0.06 \quad (1)$$

$$A_{547} = 1.79 \times (E(B - V) - 0.06) + 3.10 \times 0.06 \quad (2)$$

$$A_{814} = 1.14 \times (E(B - V) - 0.06) + 1.79 \times 0.06 \quad (3)$$

Four clusters lay outside the region for which reliable extinction values can be determined using the  $H\alpha / H\beta$  ratio, because the signal-to-noise is too low in one or both of the narrow-band images. For these clusters, we correct the photometry along the reddening vector in the color-color diagram (see Figure 6) so that the corrected photometry matches the colors predicted by theoretical models (see next section). If the cluster’s reddening vector intersects the model curve at more than one point, we use the  $\text{EW}(H\alpha)$  associated with the cluster to constrain the cluster’s age, and use the age constraint to select among the possible model points.

Correcting our images and photometry for the effects of dust using the starburst obscuration curve (Calzetti et al. 1994) provides the best agreement overall between observations and models (see Section 5). For instance, if we were to use a model of foreground dust and a standard Milky Way extinction curve (*e.g.*, Seaton 1979), we would end up with reddening vectors that are parallel to, but much longer than, those shown in Figure 4, with the result that most reddening-corrected clusters would end up with colors that are too blue to match any model. More complex dust geometries, such as a uniform mixture of dust and stars, could be appropriate for some of our clusters (*e.g.*, the youngest clusters, and those close to the dust lane). Mixed dust geometries

produce less steep reddening vectors ( $\Delta(F547M - F814W) \sim \Delta(F300W - F547M) \approx 0.5$  mag) than foreground geometries, resulting in age estimates that are  $\approx 20\%$  older. In these cases, age estimates from colors have been cross-checked against similar estimates from the  $EW(H\alpha)$ .

A general problem of using optical lines for deriving dust corrections is the potential of underestimating the amount of dust present. For foreground dust geometries this appears not to be the case, as larger dust corrections than those adopted here would again produce clusters colors that are too blue to be matched with the models. However, for those few cases where a mixed dust/star geometry is not excluded, there is a serious possibility of grossly underestimating the cluster’s intrinsic luminosity and, therefore, its mass. For these cases, our mass estimates are treated as lower limits in Table 2.

## 5. Determining Ages and Masses of the Star Clusters

We can estimate the ages and masses of the star clusters in our sample by comparing our dust-corrected photometry and  $EW(H\alpha)$  to the predicted photometry and  $EW(H\alpha)$  from population synthesis models. For the comparison, we use the Starburst99 models (Leitherer et al. 1999), which employ state-of-the-art isochrones and atmosphere calculations. We select an instantaneous burst population model covering the age range 1 Myr to 1 Gyr, with metallicity  $Z=0.040$  (to match that of M 83, Zaritsky et al. 1994; Kobulnicky et al. 1999) and a Salpeter IMF, covering stellar masses between  $1 M_{\odot}$  and  $100 M_{\odot}$ . The models include flux from continuum nebular emission for very young populations. We convolve the model SEDs with the HST filter bandpass functions to obtain HST photometry for each model point. Finally, we perform a piecewise linear interpolation between the original model points, to increase the effective photometric and age resolutions of the model.

In Figure 6, we present a two-color diagram, showing the observed and dust-corrected photometry of our cluster sample. The Starburst99 model is also plotted; age increases along the model from the upper left (bluer colors) to the lower right (redder colors). For the most part, our cluster sample follows the model prediction well, although there are nine clusters whose photometry is strikingly dissimilar from any point along the model. We discuss these outliers below. We determine the ages of the clusters in our sample by simply adopting the age of the model point whose colors are most similar to the cluster’s colors, and cross-checking the photometric age with the cluster’s  $EW(H\alpha)$ . We consider the age indeterminate if the color-distance to the nearest model point exceeds  $5\sigma$ , where  $\sigma$  characterizes the photometric errors.

There are nine clusters in our sample for which no age estimate could be made from the broadband colors. All of these clusters have  $EW(H\alpha)$  in excess of  $80 \text{ \AA}$ , indicating that they are young (age  $< 10$  Myr). With the exception of cluster # 22, their  $(m_{300} - m_{547})$  colors are 1-2 magnitudes redder than the locus of young model points. We also note that cluster # 4, with a photometric age of 72 Myr, has an  $EW(H\alpha)$ -derived age of  $\sim 6$  Myr and occupies a similar position in the two-color diagram as the nine outliers. This object is particularly interesting, because it

corresponds to a bright IR/radio source (Gallais et al. 1991), suggesting this object is even younger than our  $\text{EW}(\text{H}\alpha)$  estimate. We suspect the photometric anomalies may be related to the dust correction, for at least some of these clusters. Specifically, objects 5, 6, and 7 (the most anomalous objects in Figure 6) each lie within the large dust lane that bisects the observed region. These objects are three of the four most extinguished objects in the sample, according to our  $H\alpha/H\beta$  measurements. However, we note that no adopted extinction value or dust model can make the photometry of these objects consistent with the locus of young model points. It therefore seems likely that the dust geometry appropriate for these objects is much more complex than the geometry implied by our adopted extinction curve or other simple geometries.

There is a well-known uncertainty when applying population synthesis models to relatively small populations like these clusters. The uncertainty is caused by the stochastic effect of luminous and rare red supergiant stars. The presence of these stars causes the "red loop" visible in Figure 6. The shape and color of this loop can change dramatically in a small population, because only a few red supergiants are predicted, and random fluctuations in their actual number have a large impact on the integrated colors. However, because we find few clusters in the 10–20 Myr age range (where red supergiants dominate the integrated colors), we believe the impact of this uncertainty on our results is minimal.

In addition, there is a possible bias in cluster ages derived from  $\text{EW}(\text{H}\alpha)$  values, because the Starburst 99 models derive  $\text{EW}(\text{H}\alpha)$  under the assumption that all far-UV photons are absorbed. However, we believe this bias has only a small effect on our derived ages. Based on examining the diffused ionized gas in M 83, Calzetti et al. (1999) find that only  $\sim 10\%$  of ionizing photons escape into the general radiation field. To test the impact of this photon leakage on our cluster age estimates, we simulate full absorption of ionizing photons by artificially increasing the  $\text{EW}(\text{H}\alpha)$  of the clusters in our sample by 20%. On average, the  $\text{H}\alpha$ -derived cluster ages decreased by only 8% in this experiment.

In Figure 7, we present the distribution of our cluster age estimates from both photometry and  $\text{EW}(\text{H}\alpha)$ . Approximately 85% of the 45 clusters in our bright sample are younger than 10 Myr, and over half are in a narrow peak between 5 and 7 Myr. Figure 7 also shows the age distribution, excluding clusters less massive than  $2 \times 10^4 M_{\odot}$ . The cluster sample is complete above this mass over the entire age range of Figure 7 (see Figure 12). 75% of these massive clusters are younger than 10 Myr. The fact that the peak between 5 and 7 Myr remains significant indicates that there was an actual burst of cluster formation at that time; the peak is not just the young end of a more continuous cluster formation episode, whose older members have faded below our detection limit. Nor is it likely that such massive clusters would evaporate on timescales as short as 10 Myr.

We determine the mass of each cluster in our sample by comparing the observed, extinction-corrected flux in each filter with the predicted flux of the corresponding model point. The mass associated with the model point is renormalized to that of a Salpeter mass function over the range of stellar masses  $0.35 M_{\odot}$  to  $100 M_{\odot}$ . The lower mass cutoff provides mass estimates consistent with

a more realistic IMF with a turnover at low masses (Kroupa 2001). The flux ratio between a cluster and the corresponding model point is assumed to be equal to their mass ratio. For clusters with photometrically-determined ages, we obtain three estimates of the mass (one for each broadband filter), and adopt the mean value as the final mass estimate. For ages inferred from  $\text{EW}(\text{H}\alpha)$ , we derive the mass from the F814W magnitude only, as this is the least affected by the uncertain extinction correction. All but four of the clusters (# 4, 7, 27, and 40 in Table 2) have  $M < 10^5 M_\odot$ . Thus, the clusters in M 83 are less massive than those typically found in a major merger galaxy like the Antennae (Fritze-v. Alvensleben 1999). We present two widely divergent age and mass estimates for cluster # 4, based on its broadband photometry and its  $\text{EW}(\text{H}\alpha)$ . We consider the photometric estimate less reliable, because the nearest model point in the two-color diagram is  $4\sigma$  away, just barely within our  $5\sigma$  cut. Also, its large  $\text{EW}(\text{H}\alpha)$  is convincing evidence that the cluster must be young. The masses of 10 of the clusters are lower limits because we cannot discriminate a foreground dust geometry from a mixed gas/dust geometry (see Section 4).

We measure the half-light radii of the clusters in our sample using concentric-aperture photometry of the unconvolved F814W image. We interpolate between the apertures to find the radius that encloses half of the total flux (as measured by profile-fitting in the convolved images). Finally, we correct for the instrumental PSFs half-light radius, adopting 1.6 pixels for the F814W PC chip PSF. In Figure 8, we plot the clusters’ ages against their half-light radii. There is some indication that the older clusters tend to have smaller half-light radii, although the trend is very weak.

The results of these cluster measurements are summarized in Table 2, where the adopted color excess, the half-light radius, the cluster mass estimate, and the age estimate are listed.

## 6. The Diffuse Population

Having performed profile-fitting photometry on 45 clusters in our images, we can use the ALLSTAR routine to produce images in which the cluster light has been removed, leaving only the light of the diffuse field population. Note that for the purposes of this discussion, we consider the 330 clusters detected only in F300W to be part of the diffuse population. We determine the mean ( $m_{300} - m_{547}$ ) and ( $m_{547} - m_{814}$ ) colors of this diffuse stellar population by performing a  $5 \times 5$  blockaverage on the cluster-subtracted images, and constructing relative magnitudes from the averaged pixel values. The colors are simply the per-pixel differences in these relative magnitudes. We correct for extinction in each pixel using a similarly blockaveraged  $H\alpha/H\beta$  image, and applying the same two-component extinction model as we use on the clusters. Finally, the underlying galaxy’s red population is removed from the diffuse population colors by subtracting the average colors of the emission surrounding the starburst.

The two-color diagram for the diffuse stellar population is shown in Figure 9. Only pixels with  $\text{S/N} > 10$  in each filter are shown. The curve represents a Starburst99 model for a population with a constant star-formation rate, a Salpeter IMF covering stellar masses between 1 and  $100 M_\odot$ ,

and metallicity  $Z = 0.040$ . According to the model, most of the field is consistent with a constant star-formation rate starting 100 Myr to 1 Gyr ago, and all parts of the field contain stars that are at least 10 Myr old. This is similar to what was found in NGC 5253 (Calzetti 1997; Tremonti et al. 2001), although a much larger fraction of the field population in M 83 contains stars older than 100 Myr. In Figure 10, we show the map of the field population’s “ages”. It is important to note, these are **not** the average ages of the field populations. The model assumes that the star formation rate has been constant since some initial time  $t_0$ . The map shows the distribution of  $t_0$ . Pixels with large  $t_0$  values could still contain very young populations; so large  $t_0$  values are not necessarily inconsistent with the significant EW( $H\alpha$ ) values throughout the region (Figure 3, left panel). Without knowing how well the constant star formation rate model fits the true star formation history, it is not possible to draw strong conclusions about the distribution of ages of the diffuse populations.

With this caveat in mind, it is interesting to note the concentration of low  $t_0$  values to the west of M 83’s optical center. This area also contains five young clusters (age < 6 Myr; see Figure 11), is characterized by large values of EW( $H\alpha$ ) (Figure 3, left panel), and corresponds to the highest concentration of  $H\alpha$  flux. An area of  $1.7''$  radius around the peak nebular emission contains almost 20% of all the  $H\alpha$  emission associated with the central starburst (the total being  $\sim 7.6 \times 10^{-12} \text{ erg s}^{-1} \text{ cm}^{-2}$ ); the implied star formation rate is  $0.02 \text{ M}_\odot \text{ yr}^{-1}$  in an area of about  $55 \times 55 \text{ pc}^2$ , or about 10%–15% of the peak star formation rate per unit area found in local starbursts (Meurer et al. 1997). This region represents the largest concentration of current star formation in the core of M 83. The second large concentration of EW( $H\alpha$ ) lies nearby, on the opposite side of the dust lane. It is possible that the two observed  $H\alpha$  peaks are in reality one large star-forming area, bisected by the obscuring dust lane. The area appears to coincide with the  $10 \mu\text{m}$  emission peak reported by Telesco et al. (1993). The entire area around the northern side of the dust lane appears to be characterized by very recent, very active star formation.

## 7. Discussion: The Recent Cluster-Formation History of M 83

The bulk of the visible recent cluster formation in the central region of M 83 occurred southwest of the galaxy’s optical center, in a circumnuclear ringlet between  $3''$  and  $7''$  (54 pc and 126 pc) from the nucleus (see Figure 11). The majority of clusters more massive than  $2 \times 10^4 \text{ M}_\odot$  are between 5 and 7 Myr old, and these clusters are found throughout the active ringlet region. In contrast, the extremely young (< 4 Myr old) clusters are found preferentially along the perimeter of the ringlet region. Also, the interior of the ringlet region contains mostly low-level  $H\alpha$  emission, while its borders are lined by ridges of significant ( $\text{EW}(H\alpha) > 100$ ) emission, culminating in the large  $H\alpha$  concentration at the northern edge of the active ringlet. The three clusters with ages between 10 Myr and 30 Myr are all located around the southernmost area of the ringlet, which also corresponds to the larger of the two  $H\alpha$  bubbles identifiable in the ringlet. Clusters older than 30 Myr are all located outside the ringlet; however, we can conclude nothing about their origin

from their present location: assuming random velocities of order  $50 \text{ km s}^{-1}$  (Caldwell & Phillips 1989), the crossing time of the observed region is  $\sim 10 \text{ Myr}$ .

Star formation is clearly an ongoing process in the circumnuclear region of M 83. The location of the youngest clusters and the  $\text{H}\alpha$  morphology suggest that star formation has propagated from the interior of the ringlet to its perimeter. It appears that the 5–7 Myr population has evacuated interstellar material from most of the active ringlet region; and that star formation is continuing along the edges of the region, where the gas density is probably still high. The age sequence from the presence of relatively old (up to 25 Myr) clusters in the southern edge of the ringlet to the peak of recent star formation in the northern edge allow some tentative inference that star formation has been ongoing in the southern part of the ringlet for a longer time than in the northern part; possibly, it has been propagating from one region to the other, a conclusion already reached by Gallais et al. (1991) from near-IR images and by Puxley et al. (1997) from the CO and  $\text{Br}\gamma$  emission of the region. The starburst zone appears to be quite compact; propagation at velocities of  $\sim 10 \text{ km s}^{-1}$  would spread star formation over 150 pc in only 15 Myr.

The relationship between masses and ages for the clusters in our sample is shown in Figure 12. The 90% completeness limits impose a minimum observable mass as a function of age; this is shown as a solid curve in Figure 12. Our sample appears to be detection-limited at all ages. Therefore, we cannot say whether the lack of clusters older than 10 Myr with  $M < 2 \times 10^4 M_{\odot}$  is due to dynamical evaporation (as predicted for the centers of galaxies, Kim et al. 2000; Portegies Zwart et al. 2001), or to simple evolutionary fading of the lower-mass clusters. However, clusters more massive than  $2 \times 10^4 M_{\odot}$  are not expected to evaporate on short timescales, so the fact that most massive clusters are between 5 and 7 Myr old indicates that these clusters represent a true burst of activity, and not the young end of a continuous cluster formation rate. This model of a sharp recent starburst is also supported by the wholesale absence of dense gas across the ringlet, that explains the abnormally blue FUV spectral energy distribution observed in the center of M83 (Bonatto et al. 1998). Such a complete removal of cool interstellar matter will not necessarily last, since gas can refill the region during a sound crossing time, or about 30 Myr.

The conceptual models developed for the evolution of the center of M83 by Gallais et al. (1991) and Thatte et al. (2000) appear to apply to these HST data. Starbursts are associated with the rapid astration of molecular clouds. The material in these clouds likely is fed into the nucleus by the main bar, and possibly further shaped by an inner Lindblad resonance and the influence of a nuclear bar. When a sufficiently massive cloud complex builds up, star formation occurs, and when sufficient gas is removed, it becomes optically visible as is currently seen in M83. The masses of the molecular clouds now present in M83 of  $\sim 2 \times 10^7 M_{\odot}$  (Israel & Baas 2001) could produce a starburst comparable to that which we see, with a star formation efficiency of  $< 10\%$ . Since the cloud sizes are also a few hundred pc, the duration of the event should be 10–30 Myr. Given the lack of star clusters with ages of  $> 50 \text{ Myr}$  in our data, the typical time span between events should be longer than this, which still allows multiple bursts to occur in the last Gyr and thereby fit the diffuse stellar population colors. If each event adds about  $\sim 2 \times 10^6 M_{\odot}$  of new stars, then 10

events per Gyr would just about suffice to produce the mass in the inner 100 pc of this galaxy. Starbursts may have become a normal evolutionary event in M83.

The distribution of masses of relatively young (age  $< 10$  Myr), massive (mass  $> 10^4 M_{\odot}$ ) clusters (Figure 13) provides a look at the cluster mass function (MF) for the M 83 starburst. The observed MF is reasonably consistent with the power-law cluster MF observed in the major-merger starbursts NGC 1741 (Johnson et al. 1999) and NGC 4038/9 (Zhang & Fall 1999) ( $\Psi(M) \propto M^{-2.0}$ ). However, the mass function is based on only 25 young, massive clusters in our sample, and the dynamic range of masses is small, so the slope is only weakly constrained.

## 8. Summary

Our analysis of the HST WFPC2 images of M 83 indicates that this galaxy experienced a very recent starburst with a peak of massive cluster formation within the last 5–7 Myr, and that the starburst may have triggered even more recent star formation activity along the perimeter of the starburst region.

We measured both broadband (F300W, F547M, and F814W) and narrow-band (F656N) photometry for 45 clusters in the central 300 pc of M 83. We were able to determine the ages of 36 of these clusters by matching their positions in a two-color diagram to a Starburst99 model, and constrain the ages of the remaining nine clusters using the EW(H $\alpha$ ). Of these clusters, 39 are younger than 10 Myr, and 25 are in the narrow age range 5–7 Myr. Clusters in this age range are distributed in a semicircular annulus (the active ringlet), between 50 and 130 pc from the center of M 83. We find that the five clusters with ages younger than 4 Myr are found exclusively along the edges of the active ringlet region, suggesting an outward propagation of star formation. In addition, the presence of clusters older than 10 Myr in the southern end of the ringlet and of current, intense star formation at the northern end suggests that star formation may have started earlier in the southern region and propagated northward, in agreement with a similar inference by Gallais et al. (1991) and Puxley et al. (1997).

The look-back time on the star formation history of the starburst in M 83 is limited by the scant information provided by the few clusters older than  $\sim 10$  Myr and by the diffuse population. The latter, made mostly of a  $> 10$  Myr population, may be composed of the remnants of evaporated star clusters. The limited information available precludes us from drawing strong conclusions about the origin of the starburst in M 83. The nearly identical time evolution of the starbursts in M 83 and NGC 5253 suggests a causal connection for the starbursts, such as a galactic interaction. However, perigalacticon in this system probably occurred between 1 and 2 Gyr ago (Rogstad et al. 1974; van den Bergh 1980; Caldwell & Phillips 1989); much older than the observed burst populations. The diffuse population in M 83 perhaps offers a glimpse of what remains of star formation triggered directly by this encounter, since much of the diffuse population is consistent with a constant star-formation rate starting at least 1 Gyr ago. It is perhaps more likely that the present nuclear star

forming activity in M 83 is driven and sustained by gas inflow from its bar instability.

Acknowledgements: This work has been supported by the NASA LTSA grant NAG5-9173 and by the NASA HST grant GO-08234.01-A.

### REFERENCES

- Adelberger, K. L., & Steidel, C. C. 2000, *ApJ*, 544, 218
- Bonatto, C., Pastoriza, M. G., Alloin, D., & Bica, E. 1998, *A&A*, 334, 439
- Caldwell, N., & Phillips, M. M. 1989, *ApJ*, 338, 789
- Calzetti, D. 1997, *AJ*, 113, 162
- Calzetti, D., Armus, L., Bohlin, R. C., Kinney, A. L., Koornneef, J., & Storchi-Bergmann, T. 2000, *ApJ*, 533, 682
- Calzetti, D., Conselice, C., Gallagher, J., Harris, J., & Smith, D. A. 2001, in preparation
- Calzetti, D., Conselice, C. J., Gallagher, J. S., & Kinney, A. L. 1999, *AJ*, 118, 797
- Calzetti, D., Kinney, A. L., & Storchi-Bergmann, T. 1994, *ApJ*, 429, 582
- Calzetti, D., Meurer, G. R., Bohlin, R. C., Garnett, D. R., Kinney, A. L., Leitherer, C., & Storchi-Bergmann, T. 1997, *AJ*, 114, 1834
- Casertano, S. 1997, in *The 1997 HST Calibration Workshop with a new generation of instruments* /edited by Stefano Casertano, Robert Jedrzejewski, Charles D. Keyes, and Mark Stevens. Baltimore, MD : Space Telescope Science Institute (1997) QB 500.268 C35 1997, p. 327., 327
- Colless, M., Schade, D., Broadhurst, T. J., & Ellis, R. S. 1994, *MNRAS*, 267, 1108
- de Vaucouleurs, G. 1979, *AJ*, 84, 1270
- Elmegreen, D. M., Chromey, F. R., & Warren, A. R. 1998, *AJ*, 116, 2834
- Fritze-v. Alvensleben, U. 1999, *A&A*, 342, L25
- Gallais, P., Rouan, D., Lacombe, F., Tiphene, D., & Vauglin, I. 1991, *A&A*, 243, 309

- Heckman, T. M., Robert, C., Leitherer, C., Garnett, D. R., & van der Rydt, F. 1998, *ApJ*, 503, 646
- Israel, F. P., & Baas, F. 2001, *A&A*, 371, 433
- Johnson, K. E., Vacca, W. D., Leitherer, C., Conti, P. S., & Lipsky, S. J. 1999, *AJ*, 117, 1708
- Kennicutt, R. C., et al. 1998, *ApJ*, 498, 181
- Kim, S. S., Figer, D. F., Lee, H. M., & Morris, M. 2000, *ApJ*, 545, 301
- Kobulnicky, H. A., Kennicutt, R. C., & Pizagno, J. L. 1999, *ApJ*, 514, 544
- Kroupa, P. 2001, *MNRAS*, 322, 231
- Leitherer, C., et al. 1999, *ApJS*, 123, 3
- Lowenthal, J. D., et al. 1997, *ApJ*, 481, 673
- Meurer, G. R., Heckman, T. M., & Calzetti, D. 1999, *ApJ*, 521, 64
- Meurer, G. R., Heckman, T. M., Lehnert, M. D., Leitherer, C., & Lowenthal, J. 1997, *AJ*, 114, 54
- Osterbrock, D. E. 1989, *Astrophysics of gaseous nebulae and active galactic nuclei* (Research supported by the University of California, John Simon Guggenheim Memorial Foundation, University of Minnesota, et al. Mill Valley, CA, University Science Books, 1989, 422 p.)
- Pettini, M., Steidel, C. C., Adelberger, K. L., Dickinson, M., & Giavalisco, M. 2000, *ApJ*, 528, 96
- Phillipps, S., & Driver, S. 1995, *MNRAS*, 274, 832
- Portegies Zwart, S. F., Makino, J., McMillan, S. L. W., & Hut, P. 2001, *ApJ*, 546, L101
- Puxley, P. J., Doyon, R., & Ward, M. J. 1997, *ApJ*, 476, 120
- Rogstad, D. H., Lockart, I. A., & Wright, M. C. H. 1974, *ApJ*, 193, 309
- Schlegel, D. J., Finkbeiner, D. P., & Davis, M. 1998, *ApJ*, 500, 525
- Scowen, P. A., et al. 1998, *AJ*, 116, 163
- Seaton, M. J. 1979, *MNRAS*, 187, 73P
- Steidel, C. C., Adelberger, K. L., Giavalisco, M., Dickinson, M., & Pettini, M. 1999, *ApJ*, 519, 1
- Steidel, C. C., Giavalisco, M., Pettini, M., Dickinson, M., & Adelberger, K. L. 1996, *ApJ*, 462, L17
- Stetson, P. B. 1987, *PASP*, 99, 191
- Stetson, P. B. 1998, *PASP*, 110, 1448

- Storchi-Bergmann, T., Calzetti, D., & Kinney, A. L. 1994, *ApJ*, 429, 572
- Storchi-Bergmann, T., Kinney, A. L., & Challis, P. 1995, *ApJS*, 98, 103
- Telesco, C. M., Dressel, L. L., & Wolstencroft, R. D. 1993, *ApJ*, 414, 120
- Thatte, N., Tecza, M., & Genzel, R. 2000, *A&A*, 364, L47
- Tremonti, C. A., Calzetti, D., Leitherer, C., & Heckman, T. M. 2001, Accepted for publication in *ApJ*
- van den Bergh, S. 1980, *PASP*, 92, 122
- Voit, M., ed. 1997, *HST Data Handbook* (3.0 ed.), Vol. 1 (Space Telescope Science Institute)
- Walborn, N. R., Barbá, R. H., Brandner, W., Rubio, M. ., Grebel, E. K., & Probst, R. G. 1999, *AJ*, 117, 225
- Weedman, D. W., Wolovitz, J. B., Bershady, M. A., & Schneider, D. P. 1998, *AJ*, 116, 1643
- Whitmore, B., Heyer, I., & Casertano, S. 1999, *PASP*, 111, 1559
- Williams, R. E., et al. 1996, *AJ*, 112, 1335
- Zaritsky, D., Kennicutt, R. C., & Huchra, J. P. 1994, *ApJ*, 420, 87
- Zhang, Q., & Fall, S. M. 1999, *ApJ*, 527, L81

Table 1. Log of the Exposures<sup>a</sup>

Exposure Name	Obs. Date DD-MM-YY	Filter	Mean Wavelength (Å)	Filter Bandpass (Å)	Exposure Time (sec)
U5BG0101	25-04-00	F300W	2943.	735.8	700.
U5BG0102	25-04-00	F300W	2943.	735.8	700.
U5BG0103	25-04-00	F300W	2943.	735.8	700.
U5BG0104	25-04-00	F547M	5476.	483.1	180.
U5BG0105	25-04-00	F547M	5476.	483.1	350.
U5BG0106	25-04-00	F547M	5476.	483.1	400.
U5BG0107	25-04-00	F814W	7921.	1488.8	160.
U5BG0108	25-04-00	F814W	7921.	1488.8	200.
U5BG0109	25-04-00	F814W	7921.	1488.8	350.
U5BG0201	02-05-00	F487N	4865.	25.8	1100.
U5BG0202	02-05-00	F487N	4865.	25.8	1200.
U5BG0207	02-05-00	F487N	4865.	25.8	1000.
U5BG0208	02-05-00	F656N	6564.	21.4	600.
U5BG0209	02-05-00	F656N	6564.	21.4	600.

<sup>a</sup>The nominal telescope pointing was  $\alpha(\text{J2000})=13:37:00.75$ ,  $\delta(\text{J2000})=-29:51:57.0$  in the aperture PC1-FIX.

Table 2. Astrometry and Photometry of clusters in NGC 5236

ID	$\alpha(2000)$	$\delta(2000)$	$m_{F300W}$ (STMAG)	$m_{F547M}$ (STMAG)	$m_{F814W}$ (STMAG)	EW(H $\alpha$ ) <sup>a</sup> (Å)	E(B-V) (mag)	Mass ( $10^3 M_{\odot}$ )	Age (Myr)
1	13:36:59.80	-29:51:54.81	17.73	18.81	19.55	...	0.00	49	6.00
2	13:36:59.96	-29:51:46.34	18.42	19.20	19.84	...	0.00	27	46.67
3	13:37:00.09	-29:52:01.76	18.31	19.25	19.95	...	0.20 <sup>b</sup>	23	38.89
4	13:37:00.14	-29:51:51.08	14.86	15.40	16.30	125	0.28	48	5.79
...	...	...	...	...	...	...	...	(1074) <sup>c</sup>	(72.5) <sup>c</sup>
5	13:37:00.28	-29:51:48.39	15.88	16.13	17.34	734/968	1.20	25 <sup>d</sup>	3.07 <sup>e</sup>
6	13:37:00.32	-29:51:57.27	17.59	17.72	19.15	480	0.79	4.5 <sup>d</sup>	3.54 <sup>e</sup>
7	13:37:00.37	-29:51:48.47	14.07	14.71	16.13	1052/1670	1.42	67 <sup>d</sup>	2.22 <sup>e</sup>
8	13:37:00.37	-29:51:58.08	14.74	15.68	16.66	96	0.13	32	6.57 <sup>e</sup>
9	13:37:00.39	-29:51:59.23	16.60	17.83	18.54	39	0.00	13	6.33
10	13:37:00.40	-29:51:58.06	17.48	18.26	19.32	325	0.11	4.6	4.83 <sup>e</sup>
11	13:37:00.43	-29:51:59.31	17.82	18.52	19.52	255	0.02	4.0	5.00 <sup>e</sup>
12	13:37:00.44	-29:51:57.29	17.00	18.54	19.35	...	0.00	7.3	5.69
13	13:37:00.44	-29:51:59.53	16.04	17.28	17.92	47	0.00	23	6.50
14	13:37:00.46	-29:51:57.34	17.66	19.08	20.15	...	0.00	4.0	5.62
15	13:37:00.46	-29:51:59.72	15.85	17.33	18.50	600	0.00	20	5.50
16	13:37:00.46	-29:51:59.94	16.03	18.29	19.43	...	0.05	7.9	1.50
17	13:37:00.47	-29:51:55.18	15.64	17.32 <sup>f</sup>	18.59	408	0.05	22	5.19
18	13:37:00.49	-29:51:55.61	16.86	18.42	19.43	...	0.43	7.9 <sup>d</sup>	5.50
19	13:37:00.49	-29:52:05.10	17.63	18.59	19.22	1279	0.20 <sup>b</sup>	40	34.44
20	13:37:00.50	-29:51:57.51	18.11	19.26	19.98	...	0.16	3.4	6.00
21	13:37:00.51	-29:51:55.19	15.97	17.98	19.17	228	0.43	11 <sup>d</sup>	3.50
22	13:37:00.51	-29:51:59.97	18.01	19.90	20.58	1907	0.00	1.0	1.74 <sup>e</sup>
23	13:37:00.52	-29:51:54.75	14.41	16.68	18.09	351	0.26	36	3.00
24	13:37:00.56	-29:51:55.43	14.93	16.77	17.94	17	0.34	40	5.12
25	13:37:00.56	-29:52:00.45	15.91	17.39	18.22	1365	0.00	21	5.75
26	13:37:00.56	-29:52:01.35	14.77	16.67	18.02	43	0.00	33	3.83
27	13:37:00.58	-29:51:55.18	14.62	15.92	16.83	264/807	1.00 <sup>b</sup>	73 <sup>d</sup>	5.88
28	13:37:00.58	-29:52:01.67	16.44	18.06	19.51	81 <sup>g</sup>	0.00	0.7	6.63 <sup>e</sup>
29	13:37:00.60	-29:51:59.23	18.13	19.48	20.28	...	0.00	2.9	5.94
30	13:37:00.60	-29:52:01.20	14.96	16.69	17.87	87	0.00	41	5.19
31	13:37:00.61	-29:52:00.05	18.30	19.93	20.20	...	0.00	3.8	7.87
32	13:37:00.66	-29:51:58.02	16.82	17.88	18.68	...	0.48	12 <sup>d</sup>	6.00
33	13:37:00.67	-29:51:59.44	17.94	19.11	19.98	218	0.00	3.7	6.00
34	13:37:00.72	-29:51:57.90	16.55	18.15	19.18	239	0.21	10	5.44
35	13:37:00.73	-29:51:56.70	16.40	18.01	19.18	...	0.26	12	5.31
36	13:37:00.74	-29:51:58.05	17.08	18.56	19.88	1467	0.34	2.2	2.36 <sup>e</sup>
37	13:37:00.75	-29:51:59.50	17.32	18.71	19.04	156	0.60 <sup>b</sup>	18 <sup>d</sup>	12.67
38	13:37:00.75	-29:52:00.07	17.80	19.19	20.06	118	0.00	3.8	5.81
39	13:37:00.77	-29:52:02.12	17.74	19.14	19.88	...	0.00	4.4	6.67
40	13:37:00.82	-29:52:02.70	16.72	17.83	18.36	13	0.50	68 <sup>d</sup>	25.83
41	13:37:00.85	-29:52:03.39	18.00	19.28	19.82	...	0.00	15	18.50
42	13:37:00.88	-29:52:02.73	16.86 <sup>f</sup>	18.25	18.91	16	0.00	10	6.83
43	13:37:00.90	-29:52:02.37	17.22	18.84	19.91	...	0.00	5.5	5.44
44	13:37:00.91	-29:52:02.14	17.28	18.49	19.16	46	0.00	7.3	6.33
45	13:37:01.20	-29:51:58.53	16.02	18.02	19.39	255	0.28	9.8	3.50

<sup>a</sup>EW(H $\alpha$ ) values estimated by flux-adding all H $\alpha$  peaks within 5 and 12 pixels of the cluster position. In the three cases where the two radii yield different EW(H $\alpha$ ) values, both are presented.

<sup>b</sup>No reliable extinction estimate could be made from the H $\alpha$ /H $\beta$  map. We assume a reddening value that makes the intrinsic cluster photometry consistent with a point on the Starburst99 model.

<sup>c</sup>Probable anomalous cluster. Primary age and mass estimates are from EW(H $\alpha$ ); estimates from photometry are given in parentheses.

<sup>d</sup>We cannot exclude a mixed gas/dust geometry for objects with E(B-V)  $\gtrsim$  0.37 mag. The mass presented is a lower limit, because it assumes the intrinsic luminosity is not underestimated.

<sup>e</sup>Cluster has anomalous photometry. Age and mass estimates are from EW(H $\alpha$ ).

Table 3. Clusters Not Detected in F547M or F814W

ID	$\alpha$ (J2000)	$\delta$ (J2000)	$m_{F300W}$ (STMAG)	$m_{F547M}$ (STMAG)	E(B-V) (mag)	EW(H $\alpha$ ) ( $\text{\AA}$ )
1	13:36:59.61	-29:51:55.28	19.65	20.31	0.00	...
2	13:36:59.96	-29:51:46.35	18.42	19.20	0.00	113 <sup>a</sup>
3	13:37:00.00	-29:51:47.80	19.40	19.29	0.00	...
4	13:37:00.09	-29:52:01.77	19.08	19.69	0.00	224 <sup>a</sup>
5	13:37:00.10	-29:51:51.00	18.34	19.87	0.00	...
6	13:37:00.23	-29:52:06.34	20.05	20.40	0.00	...
7	13:37:00.34	-29:51:58.11	17.52	18.62	0.50	...
8	13:37:00.44	-29:51:59.75	15.83	17.32	0.14	...
9	13:37:00.47	-29:51:58.82	17.97	19.38	0.00	...
10	13:37:00.48	-29:51:55.62	16.20	18.71	0.43	...
11	13:37:00.48	-29:51:59.05	18.29	19.84	0.00	...
12	13:37:00.48	-29:51:54.62	16.56	18.16	0.34	158 <sup>a</sup>
13	13:37:00.49	-29:52:05.13	18.39	19.03	0.00	...
14	13:37:00.50	-29:51:55.23	16.61	18.49	0.17	757
15	13:37:00.52	-29:51:56.26	17.15	18.75	0.33	...
16	13:37:00.52	-29:52:00.75	17.87	19.47	0.00	...
17	13:37:00.54	-29:52:09.46	20.40	20.39	0.00	...
18	13:37:00.55	-29:52:09.76	19.09	20.22	0.00	...
19	13:37:00.55	-29:52:00.04	18.50	20.75	0.00	...
20	13:37:00.55	-29:52:02.37	17.36	19.48	0.16	...
21	13:37:00.56	-29:51:56.49	17.50	19.07	0.51	...
22	13:37:00.58	-29:51:55.59	16.42	18.63	0.55	...
23	13:37:00.59	-29:51:59.01	18.89	19.20	0.00	...
24	13:37:00.61	-29:52:00.75	18.41	20.21	0.00	...
25	13:37:00.61	-29:51:59.36	18.42	20.04	0.00	...
26	13:37:00.63	-29:51:58.98	17.86	19.28	0.09	...
27	13:37:00.63	-29:51:59.58	18.33	19.12	0.00	...
28	13:37:00.64	-29:51:59.31	18.32	19.60	0.00	...
29	13:37:00.66	-29:52:01.70	18.56	20.01	0.00	...
30	13:37:00.66	-29:51:59.73	17.77	19.64	0.00	...
31	13:37:00.68	-29:51:58.39	17.07	18.88	0.36	...
32	13:37:00.69	-29:52:00.16	18.49	19.78	0.00	...
33	13:37:00.70	-29:52:00.59	18.16	19.43	0.00	...
34	13:37:00.70	-29:51:58.06	16.67	18.28	0.68	...
35	13:37:00.71	-29:52:00.34	17.97	19.69	0.00	...
36	13:37:00.72	-29:51:58.34	17.11	18.65	0.35	...
37	13:37:00.72	-29:52:00.07	18.39	19.72	0.00	...
38	13:37:00.73	-29:51:56.53	17.69	19.02	0.00	...
39	13:37:00.76	-29:51:57.06	17.91	18.92	0.00	...
40	13:37:00.77	-29:51:56.80	18.28	19.09	0.00	...
41	13:37:00.77	-29:51:58.31	17.69	18.79	0.49	...
42	13:37:00.78	-29:51:57.00	18.05	19.32	0.00	...
43	13:37:00.78	-29:51:57.52	16.46	18.59	0.28	...
44	13:37:00.78	-29:51:56.66	17.97	19.12	0.00	...
45	13:37:00.80	-29:51:57.96	16.98	18.75	0.54	...
46	13:37:00.80	-29:51:57.31	17.87	19.21	0.11	...
47	13:37:00.80	-29:51:56.90	18.02	19.14	0.06	...

Table 3—Continued

ID	$\alpha$ (J2000)	$\delta$ (J2000)	$m_{F300W}$ (STMAG)	$m_{F547M}$ (STMAG)	E(B-V) (mag)	EW(H $\alpha$ ) ( $\text{\AA}$ )
48	13:37:00.80	-29:52:02.80	18.18	19.99	0.00	...
49	13:37:00.87	-29:52:03.06	18.76	20.19	0.00	...
50	13:37:00.89	-29:52:03.93	18.34	19.99	0.00	...
51	13:37:00.90	-29:51:57.20	17.85	18.89	0.17	...
52	13:37:00.92	-29:51:55.72	18.13	16.49	0.00	89
53	13:37:00.94	-29:52:04.50	18.38	19.90	0.00	...
54	13:37:00.96	-29:52:02.15	18.53	20.46	0.00	...
55	13:37:00.97	-29:52:02.79	19.03	19.86	0.00	...
56	13:37:00.97	-29:52:02.53	18.32	19.66	0.00	...
57	13:37:00.97	-29:52:01.00	20.64	20.34	0.00	...
58	13:37:01.01	-29:52:02.98	17.47	19.47	0.00	...
59	13:37:01.04	-29:52:02.46	17.66	19.81	0.00	...
60	13:37:01.05	-29:52:03.26	17.52	18.61	0.00	29
61	13:37:01.09	-29:51:57.43	18.08	19.33	0.12	...
62	13:37:01.16	-29:51:58.99	15.91	18.64	0.81	...
63	13:37:01.17	-29:51:58.50	16.63	18.12	0.79	...
64	13:37:02.04	-29:52:08.94	19.55	20.38	0.00	...
65	13:36:59.55	-29:51:59.03	20.00	...	0.00	...
66	13:36:59.67	-29:51:47.37	20.25	...	0.00	...
67	13:36:59.70	-29:51:53.32	19.78	...	0.00	...
68	13:36:59.79	-29:51:54.70	18.43	...	0.00	...
69	13:36:59.87	-29:51:58.63	20.17	...	0.00	...
70	13:36:59.89	-29:51:49.46	19.45	...	0.16	...
71	13:36:59.96	-29:51:48.29	19.33	...	0.00	...
72	13:36:59.99	-29:51:47.71	19.36	...	0.00	...
73	13:37:00.05	-29:51:50.81	19.52	...	0.00	...
74	13:37:00.09	-29:51:50.26	19.38	...	0.22	...
75	13:37:00.10	-29:51:50.76	18.58	...	0.00	...
76	13:37:00.10	-29:51:51.34	19.23	...	0.00	...
77	13:37:00.12	-29:51:50.78	19.26	...	0.00	...
78	13:37:00.13	-29:51:51.26	18.68	...	0.00	...
79	13:37:00.14	-29:51:51.49	17.85	...	0.53	...
80	13:37:00.15	-29:51:50.68	17.89	...	0.42	...
81	13:37:00.18	-29:51:51.11	18.14	...	0.76	834
82	13:37:00.19	-29:51:44.22	19.90	...	0.00	...
83	13:37:00.35	-29:52:00.78	18.53	...	0.37	...
84	13:37:00.37	-29:51:58.52	17.67	...	0.39	...
85	13:37:00.38	-29:51:58.55	17.72	...	0.41	...
86	13:37:00.38	-29:51:59.24	18.01	...	0.11	...
87	13:37:00.39	-29:51:57.65	18.30	...	0.21	...
88	13:37:00.39	-29:51:58.19	17.66	...	0.01	...
89	13:37:00.40	-29:51:56.85	17.89	...	0.34	...
90	13:37:00.40	-29:51:58.00	17.74	...	0.11	...
91	13:37:00.42	-29:51:59.66	17.71	...	0.23	...
92	13:37:00.42	-29:51:57.55	18.21	...	0.37	...
93	13:37:00.42	-29:51:57.00	18.42	...	0.17	...
94	13:37:00.43	-29:51:57.23	18.45	...	0.26	...

Table 3—Continued

ID	$\alpha$ (J2000)	$\delta$ (J2000)	$m_{F300W}$ (STMAG)	$m_{F547M}$ (STMAG)	E(B-V) (mag)	EW(H $\alpha$ ) ( $\text{\AA}$ )
95	13:37:00.43	-29:51:59.08	18.15	...	0.18	...
96	13:37:00.43	-29:51:59.53	17.31	...	0.12	...
97	13:37:00.43	-29:51:58.19	17.22	...	0.30	397
98	13:37:00.43	-29:52:00.11	18.82	...	0.19	...
99	13:37:00.44	-29:51:56.97	18.98	...	0.00	...
100	13:37:00.44	-29:51:57.51	19.83	...	0.04	...
101	13:37:00.44	-29:52:00.99	17.90	...	0.31	...
102	13:37:00.45	-29:51:58.70	18.14	...	0.00	...
103	13:37:00.45	-29:51:58.94	17.93	...	0.11	...
104	13:37:00.45	-29:51:55.60	17.15	...	0.58	...
105	13:37:00.45	-29:51:58.04	18.45	...	0.01	...
106	13:37:00.45	-29:51:59.40	17.86	...	0.00	...
107	13:37:00.46	-29:52:01.26	18.92	...	0.28	...
108	13:37:00.47	-29:51:58.65	18.38	...	0.00	...
109	13:37:00.47	-29:51:59.70	17.19	...	0.00	...
110	13:37:00.47	-29:51:54.37	16.57	...	0.91	3120
111	13:37:00.47	-29:51:55.02	17.32	...	0.10	...
112	13:37:00.47	-29:51:59.43	18.45	...	0.00	...
113	13:37:00.47	-29:52:00.18	16.74	...	0.34	...
114	13:37:00.48	-29:51:56.57	18.05	...	0.42	...
115	13:37:00.48	-29:51:55.53	17.11	...	0.25	...
116	13:37:00.48	-29:51:54.93	16.77	...	0.22	...
117	13:37:00.48	-29:52:00.59	17.65	...	0.26	...
118	13:37:00.48	-29:51:54.62	16.56	...	0.34	...
119	13:37:00.48	-29:51:58.23	19.06	...	0.01	...
120	13:37:00.49	-29:51:59.27	17.80	...	0.00	210
121	13:37:00.49	-29:52:00.03	17.86	...	0.13	...
122	13:37:00.49	-29:51:59.80	18.08	...	0.01	...
123	13:37:00.49	-29:51:59.53	18.36	...	0.00	...
124	13:37:00.50	-29:51:59.77	18.21	...	0.00	...
125	13:37:00.50	-29:52:00.32	18.14	...	0.08	...
126	13:37:00.50	-29:52:01.44	19.16	...	0.04	...
127	13:37:00.50	-29:51:54.67	16.59	...	0.35	...
128	13:37:00.50	-29:51:59.02	18.36	...	0.00	...
129	13:37:00.50	-29:51:58.58	19.03	...	0.00	...
130	13:37:00.50	-29:52:00.70	18.12	...	0.00	...
131	13:37:00.50	-29:51:55.44	17.31	...	0.30	...
132	13:37:00.51	-29:51:59.55	17.99	...	0.00	...
133	13:37:00.51	-29:52:00.50	18.02	...	0.00	...
134	13:37:00.51	-29:52:00.80	18.11	...	0.00	...
135	13:37:00.52	-29:51:55.54	16.60	...	0.50	...
136	13:37:00.52	-29:51:59.13	19.36	...	0.00	...
137	13:37:00.52	-29:51:54.33	17.52	...	0.51	...
138	13:37:00.52	-29:52:00.27	18.14	...	0.00	...
139	13:37:00.52	-29:51:55.81	17.33	...	0.58	...
140	13:37:00.52	-29:52:01.05	18.34	...	0.00	...
141	13:37:00.52	-29:52:01.42	19.65	...	0.00	...

Table 3—Continued

ID	$\alpha$ (J2000)	$\delta$ (J2000)	$m_{F300W}$ (STMAG)	$m_{F547M}$ (STMAG)	E(B-V) (mag)	EW(H $\alpha$ ) ( $\text{\AA}$ )
142	13:37:00.53	-29:51:55.17	17.23	...	0.45	...
143	13:37:00.53	-29:51:54.62	17.16	...	0.45	...
144	13:37:00.53	-29:51:59.56	19.63	...	0.00	...
145	13:37:00.54	-29:52:01.75	17.98	...	0.24	...
146	13:37:00.54	-29:51:58.89	19.60	...	0.00	...
147	13:37:00.54	-29:51:54.79	16.77	...	0.44	...
148	13:37:00.54	-29:52:00.01	18.68	...	0.00	...
149	13:37:00.54	-29:52:00.86	17.81	...	0.00	...
150	13:37:00.54	-29:52:00.39	18.65	...	0.00	...
151	13:37:00.55	-29:51:59.21	18.98	...	0.00	...
152	13:37:00.55	-29:52:00.56	17.75	...	0.00	...
153	13:37:00.55	-29:51:58.67	18.39	...	0.00	...
154	13:37:00.56	-29:51:58.87	18.74	...	0.00	...
155	13:37:00.56	-29:51:59.63	18.80	...	0.00	...
156	13:37:00.56	-29:52:00.60	19.41	...	0.00	...
157	13:37:00.56	-29:51:53.42	14.02	...	1.32	...
158	13:37:00.57	-29:51:55.21	17.11	...	0.54	...
159	13:37:00.57	-29:51:59.94	19.17	...	0.00	...
160	13:37:00.57	-29:52:00.86	17.67	...	0.00	14
161	13:37:00.57	-29:51:59.09	19.54	...	0.00	...
162	13:37:00.58	-29:51:58.70	18.48	...	0.00	...
163	13:37:00.58	-29:52:00.22	18.56	...	0.00	...
164	13:37:00.58	-29:51:59.35	19.54	...	0.00	...
165	13:37:00.58	-29:52:00.44	18.91	...	0.00	...
166	13:37:00.59	-29:52:01.50	17.27	...	0.00	...
167	13:37:00.59	-29:52:01.95	18.24	...	0.12	...
168	13:37:00.59	-29:52:00.69	18.81	...	0.00	...
169	13:37:00.59	-29:51:59.83	19.05	...	0.00	...
170	13:37:00.60	-29:52:00.24	18.60	...	0.00	...
171	13:37:00.60	-29:52:01.75	17.54	...	0.00	...
172	13:37:00.60	-29:51:59.47	19.64	...	0.00	...
173	13:37:00.60	-29:51:55.60	16.81	...	0.61	...
174	13:37:00.60	-29:52:03.64	20.30	...	0.22	...
175	13:37:00.61	-29:52:01.58	18.41	...	0.18	...
176	13:37:00.61	-29:51:59.81	19.06	...	0.00	...
177	13:37:00.61	-29:52:04.54	21.02	...	0.00	...
178	13:37:00.62	-29:52:01.42	17.50	...	0.00	...
179	13:37:00.62	-29:51:55.56	17.08	...	0.61	...
180	13:37:00.62	-29:51:58.80	17.65	...	0.15	...
181	13:37:00.62	-29:52:00.30	18.84	...	0.00	...
182	13:37:00.62	-29:52:01.66	17.34	...	0.12	...
183	13:37:00.63	-29:52:00.60	19.66	...	0.00	...
184	13:37:00.63	-29:52:00.92	18.76	...	0.00	...
185	13:37:00.63	-29:52:01.21	17.94	...	0.00	...
186	13:37:00.63	-29:52:00.03	18.74	...	0.00	...
187	13:37:00.63	-29:52:03.73	19.38	...	0.16	...
188	13:37:00.63	-29:51:59.69	18.44	...	0.00	...

Table 3—Continued

ID	$\alpha$ (J2000)	$\delta$ (J2000)	$m_{F300W}$ (STMAG)	$m_{F547M}$ (STMAG)	E(B-V) (mag)	EW(H $\alpha$ ) ( $\text{\AA}$ )
189	13:37:00.64	-29:51:59.72	18.47	...	0.00	...
190	13:37:00.64	-29:52:00.24	18.76	...	0.00	...
191	13:37:00.65	-29:51:58.11	16.85	...	0.60	...
192	13:37:00.65	-29:52:01.30	19.07	...	0.00	...
193	13:37:00.66	-29:51:59.45	18.38	...	0.00	...
194	13:37:00.66	-29:52:00.11	18.54	...	0.00	...
195	13:37:00.66	-29:51:56.65	16.74	...	0.94	559
196	13:37:00.66	-29:52:03.15	19.21	...	0.00	...
197	13:37:00.67	-29:52:01.84	18.86	...	0.00	...
198	13:37:00.67	-29:52:02.87	18.65	...	0.00	...
199	13:37:00.68	-29:51:58.28	18.18	...	0.28	...
200	13:37:00.68	-29:52:00.51	18.98	...	0.00	...
201	13:37:00.68	-29:52:00.81	19.21	...	0.01	...
202	13:37:00.68	-29:52:00.16	18.32	...	0.00	...
203	13:37:00.69	-29:51:59.73	18.74	...	0.00	...
204	13:37:00.69	-29:52:02.36	19.41	...	0.05	...
205	13:37:00.69	-29:51:57.20	18.08	...	0.62	...
206	13:37:00.69	-29:52:01.79	19.47	...	0.00	...
207	13:37:00.70	-29:52:01.38	18.89	...	0.00	...
208	13:37:00.70	-29:52:04.93	19.35	...	0.00	...
209	13:37:00.70	-29:52:00.96	19.05	...	0.00	...
210	13:37:00.71	-29:51:56.49	16.67	...	0.61	...
211	13:37:00.71	-29:52:02.62	19.79	...	0.00	...
212	13:37:00.71	-29:52:01.98	19.36	...	0.00	...
213	13:37:00.72	-29:52:01.71	19.12	...	0.00	...
214	13:37:00.72	-29:51:56.75	17.82	...	0.26	...
215	13:37:00.72	-29:52:03.02	21.01	...	0.08	...
216	13:37:00.72	-29:51:57.25	17.45	...	0.66	...
217	13:37:00.72	-29:52:00.65	18.80	...	0.00	...
218	13:37:00.72	-29:52:02.25	19.21	...	0.00	...
219	13:37:00.73	-29:52:01.87	18.59	...	0.00	...
220	13:37:00.73	-29:52:01.60	19.68	...	0.00	...
221	13:37:00.73	-29:52:02.61	18.70	...	0.00	...
222	13:37:00.74	-29:51:56.57	18.43	...	0.00	...
223	13:37:00.75	-29:51:56.40	18.13	...	0.04	...
224	13:37:00.75	-29:51:56.96	17.34	...	0.37	...
225	13:37:00.75	-29:52:02.41	20.08	...	0.00	...
226	13:37:00.75	-29:51:56.11	16.70	...	0.54	...
227	13:37:00.75	-29:51:58.30	17.33	...	0.42	...
228	13:37:00.76	-29:52:02.06	19.62	...	0.00	...
229	13:37:00.76	-29:51:57.50	17.11	...	0.43	...
230	13:37:00.76	-29:52:01.70	19.52	...	0.00	...
231	13:37:00.77	-29:51:56.49	18.25	...	0.00	...
232	13:37:00.77	-29:51:58.64	17.78	...	0.36	...
233	13:37:00.77	-29:52:04.90	19.15	...	0.00	...
234	13:37:00.77	-29:52:00.92	19.24	...	0.06	...
235	13:37:00.78	-29:51:56.21	18.20	...	0.00	...

Table 3—Continued

ID	$\alpha$ (J2000)	$\delta$ (J2000)	$m_{F300W}$ (STMAG)	$m_{F547M}$ (STMAG)	E(B-V) (mag)	EW(H $\alpha$ ) ( $\text{\AA}$ )
236	13:37:00.78	-29:51:57.83	18.14	...	0.45	...
237	13:37:00.78	-29:52:01.20	20.06	...	0.00	...
238	13:37:00.79	-29:52:02.27	18.78	...	0.00	...
239	13:37:00.80	-29:51:58.38	18.67	...	0.47	...
240	13:37:00.80	-29:52:02.06	18.95	...	0.00	...
241	13:37:00.81	-29:51:47.10	20.07	...	0.00	...
242	13:37:00.81	-29:52:03.06	18.95	...	0.00	...
243	13:37:00.82	-29:52:05.67	20.60	...	0.00	...
244	13:37:00.82	-29:52:02.58	19.10	...	0.00	...
245	13:37:00.82	-29:51:57.51	18.08	...	0.35	...
246	13:37:00.82	-29:52:02.33	19.08	...	0.00	...
247	13:37:00.83	-29:52:01.39	19.66	...	0.00	...
248	13:37:00.83	-29:52:03.03	19.22	...	0.00	...
249	13:37:00.84	-29:52:01.63	18.86	...	0.00	...
250	13:37:00.84	-29:52:01.97	19.36	...	0.00	...
251	13:37:00.84	-29:52:02.48	19.30	...	0.00	...
252	13:37:00.85	-29:52:01.05	19.45	...	0.00	...
253	13:37:00.85	-29:51:57.69	18.21	...	0.22	...
254	13:37:00.85	-29:52:06.04	19.37	...	0.26	...
255	13:37:00.85	-29:52:03.14	18.95	...	0.00	...
256	13:37:00.86	-29:51:57.88	18.08	...	0.32	...
257	13:37:00.86	-29:52:02.05	19.09	...	0.00	...
258	13:37:00.87	-29:52:01.48	19.33	...	0.00	...
259	13:37:00.87	-29:52:03.30	18.83	...	0.00	...
260	13:37:00.87	-29:52:03.81	19.21	...	0.00	...
261	13:37:00.88	-29:51:57.48	18.57	...	0.14	...
262	13:37:00.88	-29:52:02.68	18.19	...	0.00	...
263	13:37:00.88	-29:52:04.79	18.54	...	0.00	...
264	13:37:00.89	-29:52:03.58	19.37	...	0.00	...
265	13:37:00.89	-29:52:01.77	20.32	...	0.00	...
266	13:37:00.89	-29:51:59.65	19.47	...	0.00	...
267	13:37:00.90	-29:52:01.51	19.32	...	0.00	...
268	13:37:00.90	-29:52:04.29	18.70	...	0.00	...
269	13:37:00.90	-29:52:02.52	18.71	...	0.00	...
270	13:37:00.90	-29:52:03.19	19.22	...	0.00	...
271	13:37:00.91	-29:52:01.25	19.71	...	0.00	...
272	13:37:00.91	-29:51:59.58	18.29	...	0.20	...
273	13:37:00.91	-29:52:01.90	19.58	...	0.00	...
274	13:37:00.92	-29:52:03.90	18.57	...	0.00	...
275	13:37:00.92	-29:52:03.21	18.75	...	0.00	...
276	13:37:00.92	-29:52:04.24	18.67	...	0.00	...
277	13:37:00.92	-29:52:04.73	18.15	...	0.21	...
278	13:37:00.93	-29:52:03.53	19.58	...	0.00	...
279	13:37:00.93	-29:52:00.12	19.01	...	0.00	...
280	13:37:00.93	-29:52:02.88	19.29	...	0.00	...
281	13:37:00.94	-29:52:01.14	19.50	...	0.00	...
282	13:37:00.94	-29:51:59.66	19.61	...	0.01	...

Table 3—Continued

ID	$\alpha$ (J2000)	$\delta$ (J2000)	$m_{F300W}$ (STMAG)	$m_{F547M}$ (STMAG)	E(B-V) (mag)	EW(H $\alpha$ ) ( $\text{\AA}$ )
283	13:37:00.94	-29:52:00.83	19.17	...	0.00	...
284	13:37:00.95	-29:52:03.18	19.17	...	0.00	...
285	13:37:00.96	-29:52:00.18	19.11	...	0.19	...
286	13:37:00.96	-29:52:01.21	18.62	...	0.09	...
287	13:37:00.96	-29:51:59.83	18.79	...	0.19	...
288	13:37:00.97	-29:52:02.20	19.18	...	0.00	...
289	13:37:00.98	-29:52:02.82	18.94	...	0.00	...
290	13:37:00.98	-29:52:04.17	19.24	...	0.00	...
291	13:37:00.98	-29:52:02.41	18.27	...	0.00	...
292	13:37:00.98	-29:52:03.05	17.99	...	0.00	...
293	13:37:00.99	-29:52:03.42	18.62	...	0.00	...
294	13:37:00.99	-29:52:04.02	19.44	...	0.00	...
295	13:37:00.99	-29:52:01.01	19.73	...	0.00	...
296	13:37:01.00	-29:52:03.21	17.77	...	0.00	...
297	13:37:01.01	-29:52:02.13	18.44	...	0.00	...
298	13:37:01.01	-29:52:02.54	17.92	...	0.00	...
299	13:37:01.01	-29:52:03.41	17.90	...	0.00	...
300	13:37:01.02	-29:52:02.40	18.13	...	0.00	...
301	13:37:01.02	-29:52:03.15	17.56	...	0.00	...
302	13:37:01.02	-29:52:02.64	18.08	...	0.00	...
303	13:37:01.03	-29:52:02.93	17.66	...	0.00	...
304	13:37:01.03	-29:52:00.05	19.84	...	0.00	...
305	13:37:01.03	-29:52:03.40	17.80	...	0.00	...
306	13:37:01.04	-29:52:02.14	18.38	...	0.00	...
307	13:37:01.04	-29:52:03.13	17.43	...	0.00	...
308	13:37:01.05	-29:52:02.74	17.77	...	0.00	...
309	13:37:01.05	-29:52:02.94	17.75	...	0.00	...
310	13:37:01.06	-29:52:02.55	18.15	...	0.00	...
311	13:37:01.06	-29:52:03.22	18.36	...	0.00	...
312	13:37:01.07	-29:52:02.29	18.28	...	0.00	...
313	13:37:01.07	-29:52:01.76	18.30	...	0.02	...
314	13:37:01.07	-29:52:02.75	17.94	...	0.00	...
315	13:37:01.08	-29:52:02.12	18.30	...	0.00	...
316	13:37:01.08	-29:51:40.85	20.34	...	0.00	...
317	13:37:01.08	-29:52:01.34	17.39	...	0.24	...
318	13:37:01.08	-29:52:03.00	18.60	...	0.00	...
319	13:37:01.11	-29:51:59.71	19.13	...	0.19	...
320	13:37:01.13	-29:51:53.46	20.31	...	0.00	...
321	13:37:01.13	-29:51:59.30	19.28	...	0.06	...
322	13:37:01.18	-29:51:58.62	17.19	...	0.42	...
323	13:37:01.21	-29:51:55.72	19.36	...	0.00	...
324	13:37:01.24	-29:51:57.44	18.20	...	0.35	...
325	13:37:01.25	-29:51:56.88	18.73	...	0.26	...
326	13:37:01.38	-29:52:05.44	20.65	...	0.00	...
327	13:37:01.38	-29:52:10.33	20.50	...	0.00	...
328	13:37:01.59	-29:51:57.47	19.81	...	0.00	...
329	13:37:01.70	-29:51:40.49	20.25	...	0.00	...

Table 3—Continued

ID	$\alpha$ (J2000)	$\delta$ (J2000)	$m_{F300W}$ (STMAG)	$m_{F547M}$ (STMAG)	E(B-V) (mag)	EW(H $\alpha$ ) ( $\text{\AA}$ )
330	13:37:02.00	-29:51:57.36	20.16	...	0.00	...

<sup>a</sup>EW(H $\alpha$ ) value estimated from flux measured through an 11-pixel aperture in the peak-subtracted F656N image.

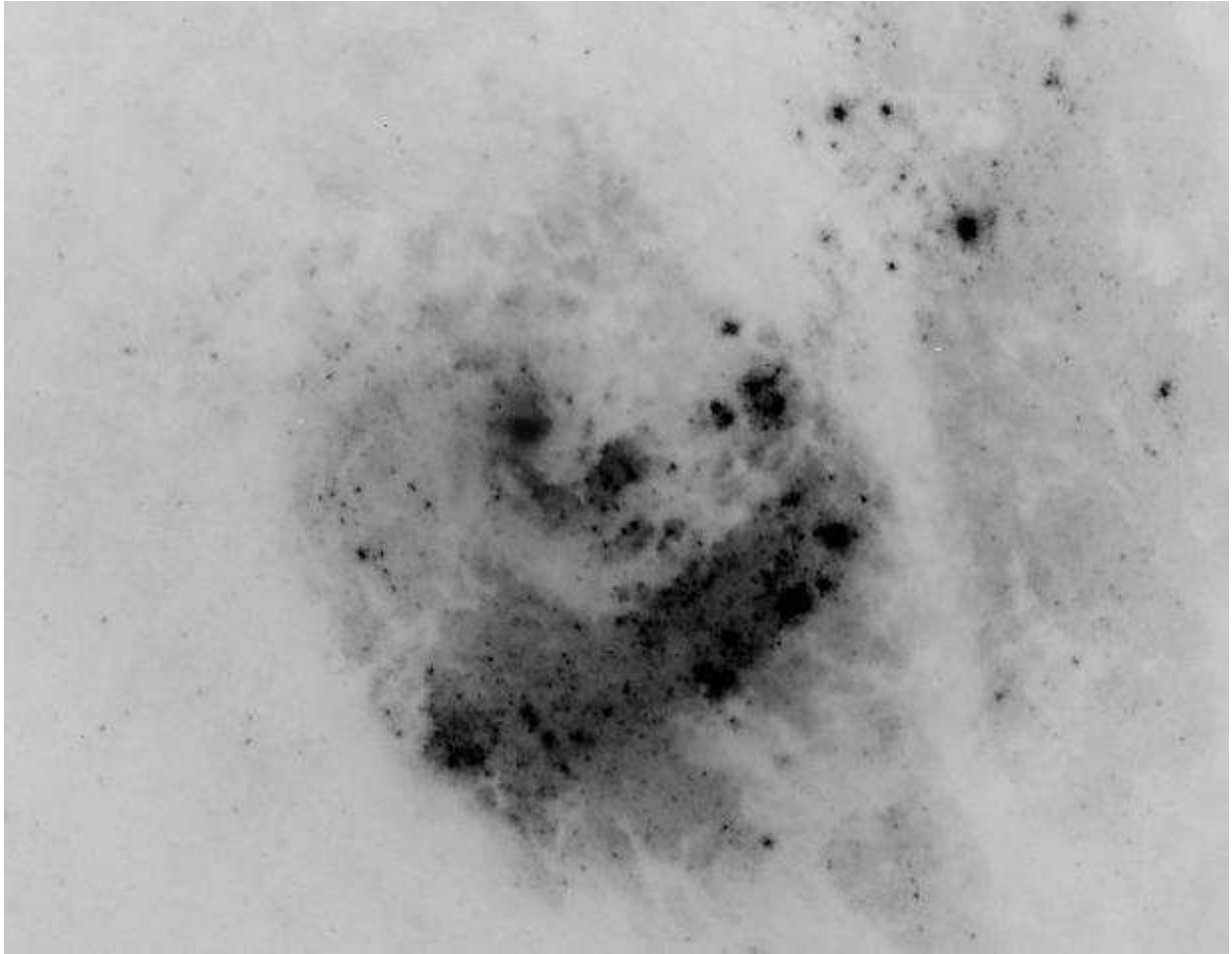


Fig. 1.— F547M exposure of M 83. North is at the top, and East is at the left. (for a color composite image, see <http://www.stsci.edu/~jharris/m83color.png>)

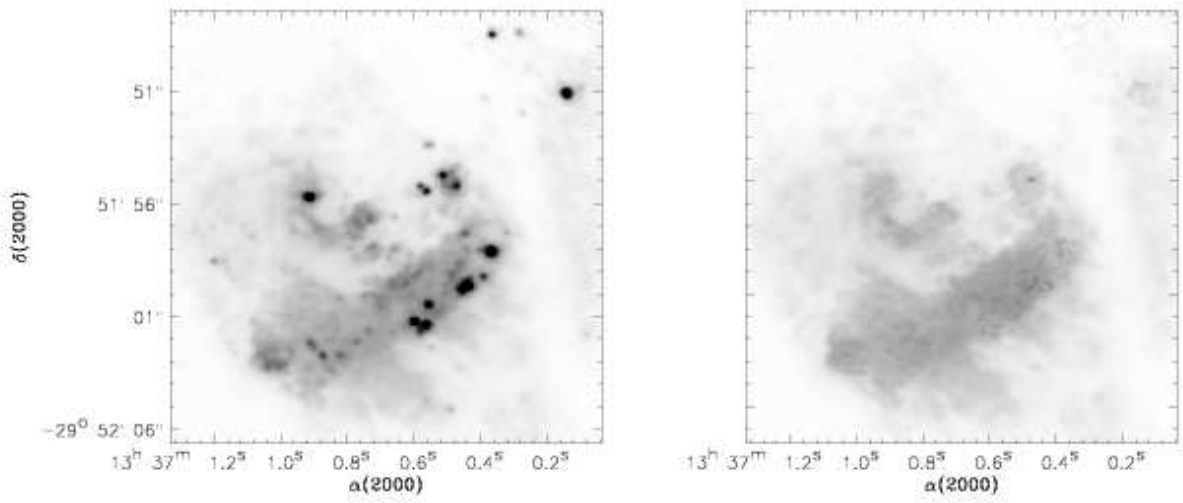


Fig. 2.— **Left:** the F547M image of the central starburst in M 83, convolved with a  $\sigma = 2$  pixel Gaussian kernel. North is at the top, and east is to the left. The bright peak near  $13^h 37^m 0.9^s$ ,  $-29^\circ 51' 55''$  is the optical nucleus of the galaxy. The prominent dust lane can also be seen running north-south, in the western part of the region. **Right:** the same image, after all detected objects have been fit and subtracted by DAOPHOT and ALLSTAR.

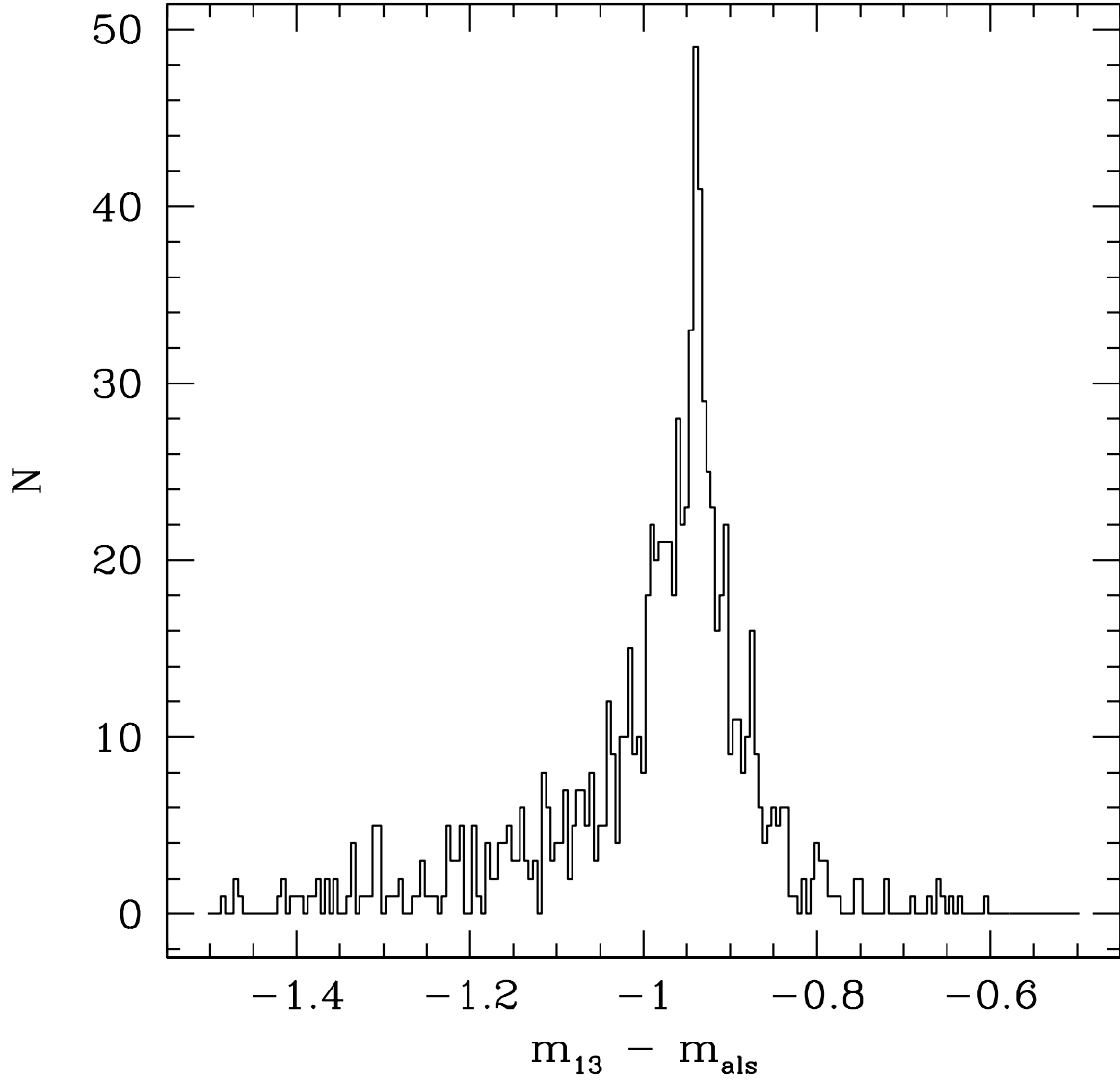


Fig. 3.— A histogram of the aperture corrections derived from artificial clusters added to isolated regions of the F547M image. The aperture correction is defined as the difference between the 13-pixel aperture magnitude and the allstar magnitude. We determine the mean aperture correction by fitting a Gaussian function to the histogram peak, and adopt the width of the peak as the contribution of the aperture correction to the photometric errors.

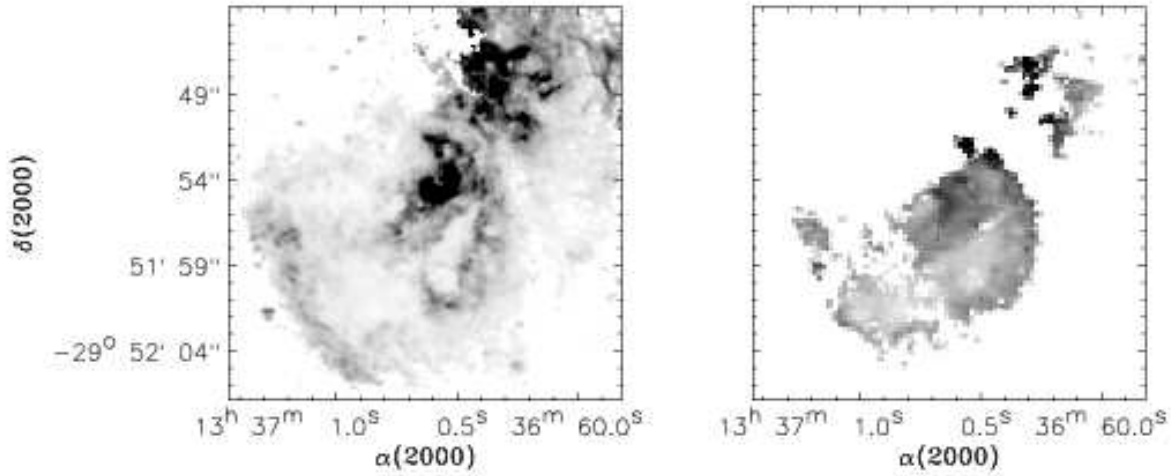


Fig. 4.— **Left:** A map of the  $\text{EW}(H\alpha)$  in the core of M 83. Pixel values range from zero (white) to over 1000 (black). **Right:** A map of the  $H\alpha/H\beta$  ratio for the observed region of M 83. Pixel values range from zero (white) to 10 (black). We use this ratio to estimate the dust extinction in each broadband image, as explained in the text. The large gap in the northwest region of the map corresponds to the prominent dust lane, where signal in the narrow-band images is lost due to heavy extinction.

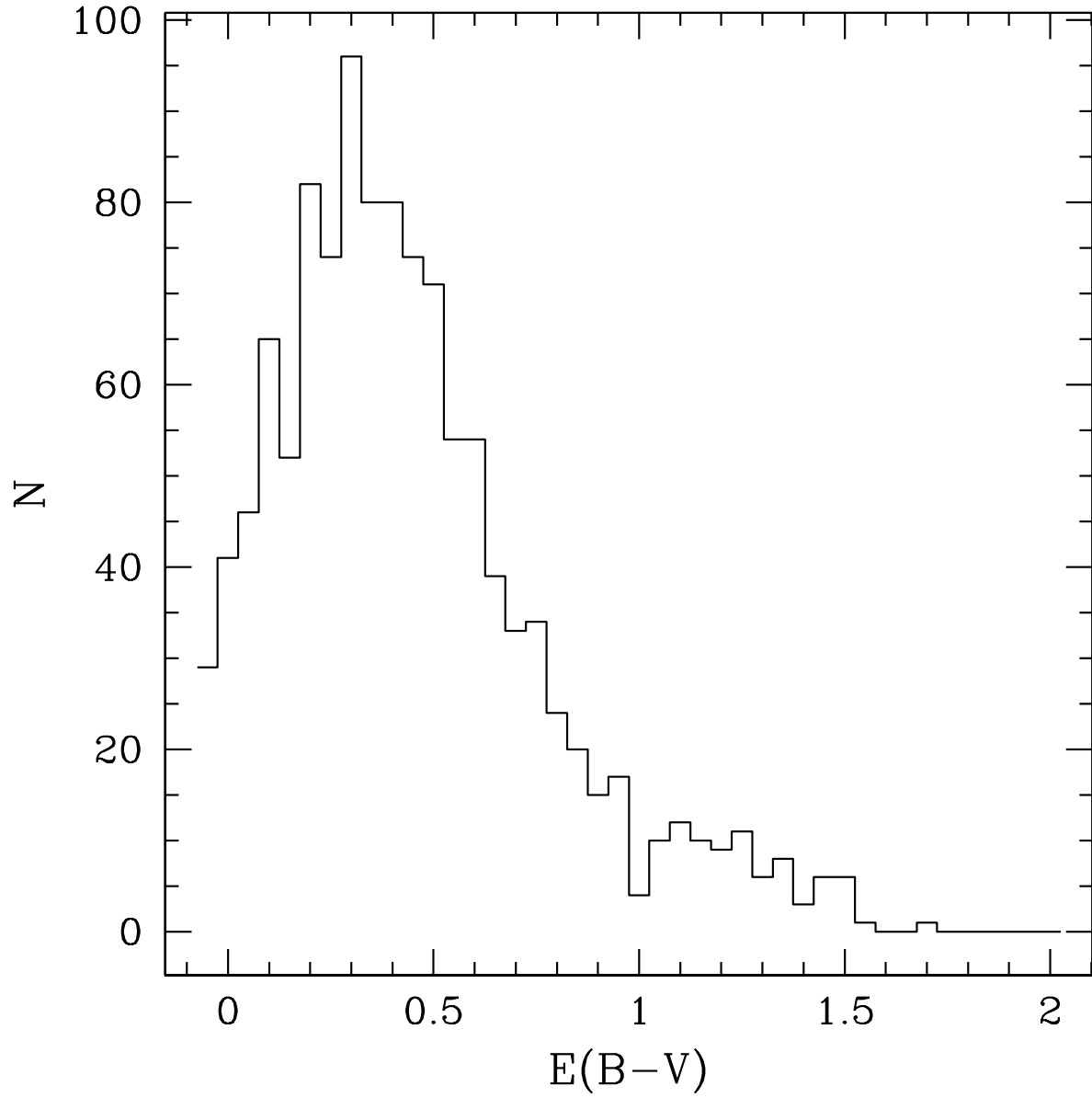


Fig. 5.— The distribution of  $E(B-V)$  reddening values, as inferred from the  $H\alpha/H\beta$  ratio image (see Figure 4).

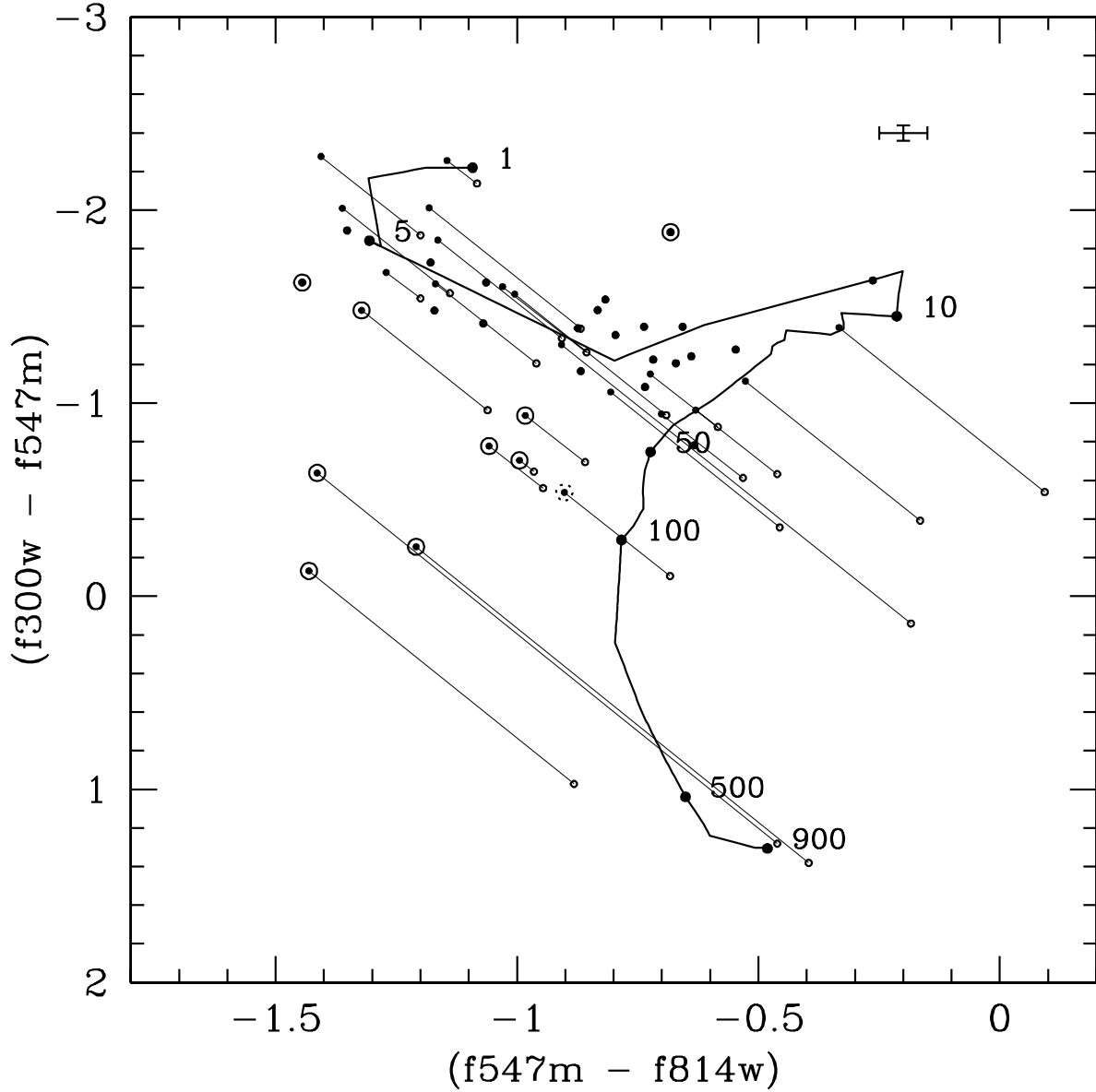


Fig. 6.— A two-color diagram ( $m_{547} - m_{814}$  vs.  $m_{300} - m_{547}$ ), illustrating our cluster photometry. Each cluster is represented by a pair of points, representing the observed (open points) and extinction-corrected (solid points) photometry. The pair of points is connected by a line, for clarity. The curve is the photometry of a Starburst99 population model with  $Z=0.04$ , a Salpeter IMF, and an instantaneous burst star formation history. The model is a sequence in age; various ages are labeled (in Myr) along the curve. The mean photometric error for our cluster sample is indicated by the error bars in the upper right corner. The nine clusters whose extinction-corrected colors are more than  $5\sigma$  from any model point are indicated with large circles. Object #4, whose photometry is *nearly*  $5\sigma$  from the model, is indicated with a dotted circle.

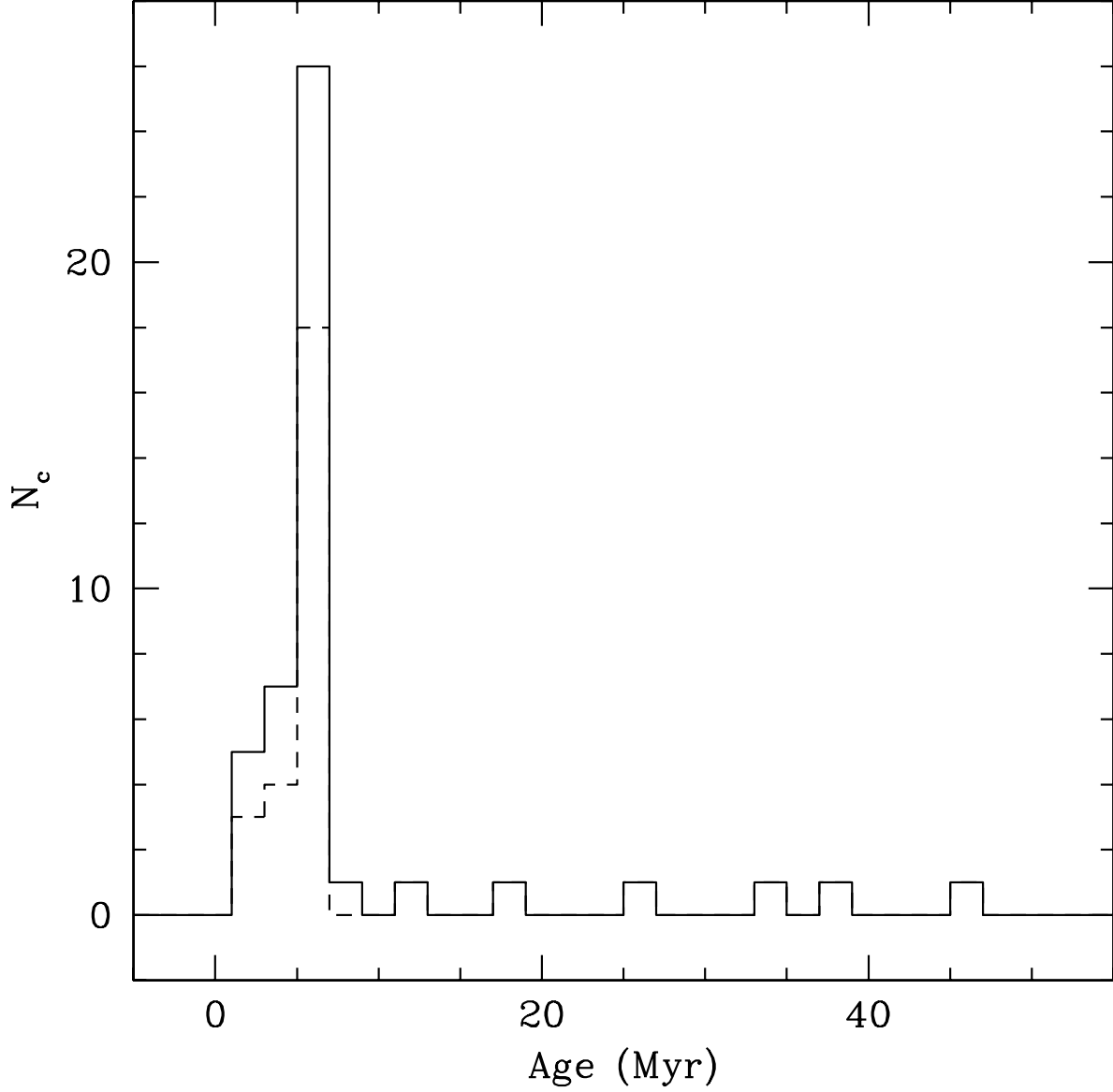


Fig. 7.— The distribution of estimated ages for the clusters in our sample. The dashed line is the distribution of ages, excluding clusters with  $M < 2 \times 10^4 M_{\odot}$ . Since our sample is complete to this mass over the entire age range (see Figure 12), the fact that the strong peak at 5–7 Myr remains indicates that there was an actual burst of activity at this time, as opposed to it being the young end of a more continuous cluster formation episode.

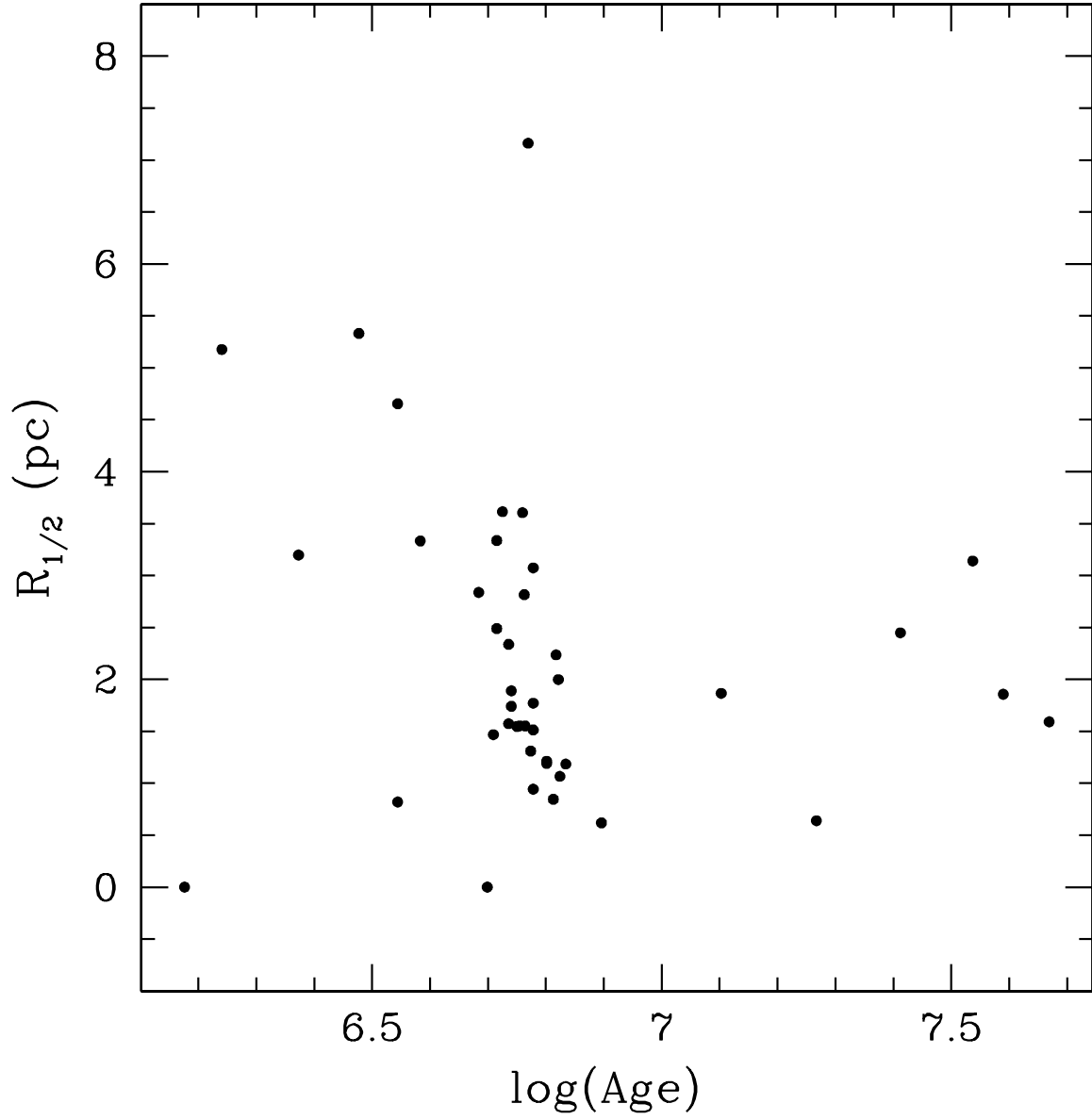


Fig. 8.— The clusters’ half-light radii plotted against their age. The half-light radius is derived for each cluster from the F814W image.

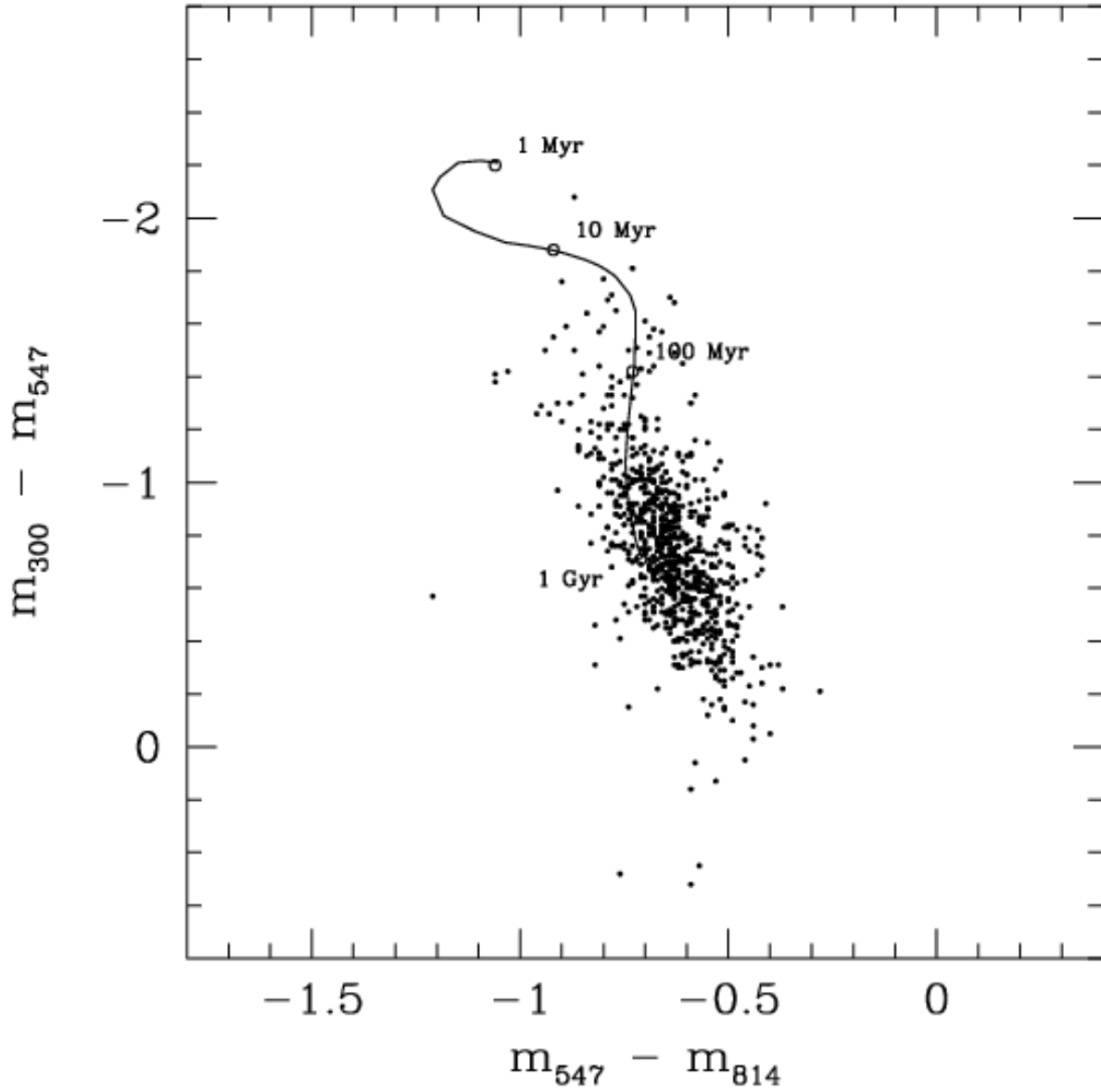


Fig. 9.— The two-color diagram for the unresolved field population in the M 83 starburst. Each point represents the colors of a  $5 \times 5$  blockaveraged pixel in the cluster-subtracted images. The curve is the photometry of a starburst99 population model with  $Z=0.04$ , a Salpeter IMF, and a constant SFR. Various ages along the model are labeled (in Myr), the ages correspond to the time at which the constant star formation rate began.

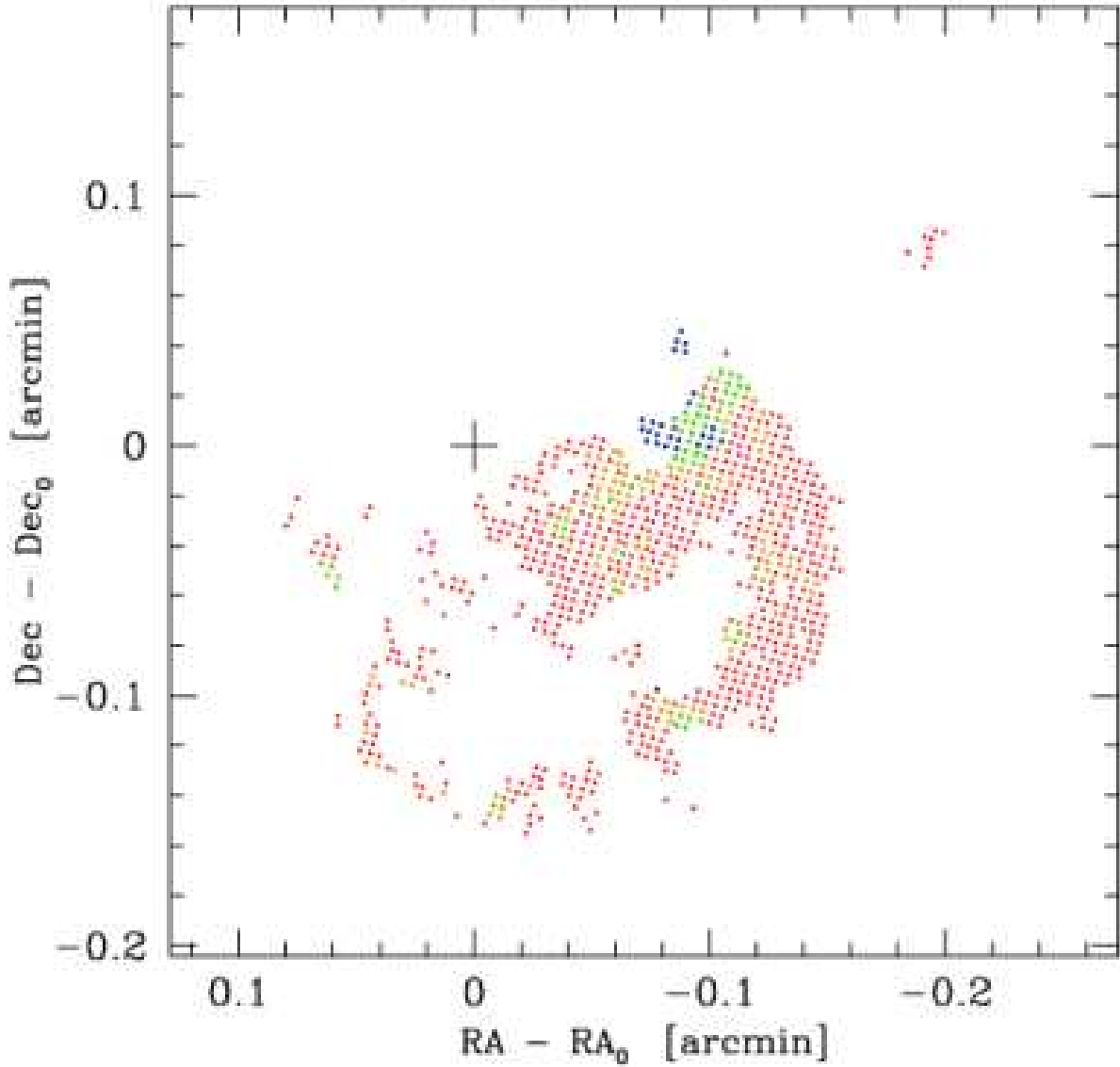


Fig. 10.— A map of the ages of the oldest stars in the diffuse field population, based on fitting the per-pixel colors of the field to a constant star-formation rate model (see Figure 9). The points are color-coded by age: 10–100 Myr (blue), 100–250 Myr (green), 250–500 Myr (yellow), and 500–1000 Myr (red). The field is generally consistent with constant star formation since at least 1 Gyr ago, although one region is better fit by a much younger initial age. This region corresponds to a group of six young clusters, and one of the two concentrations of large EW(H $\alpha$ ).



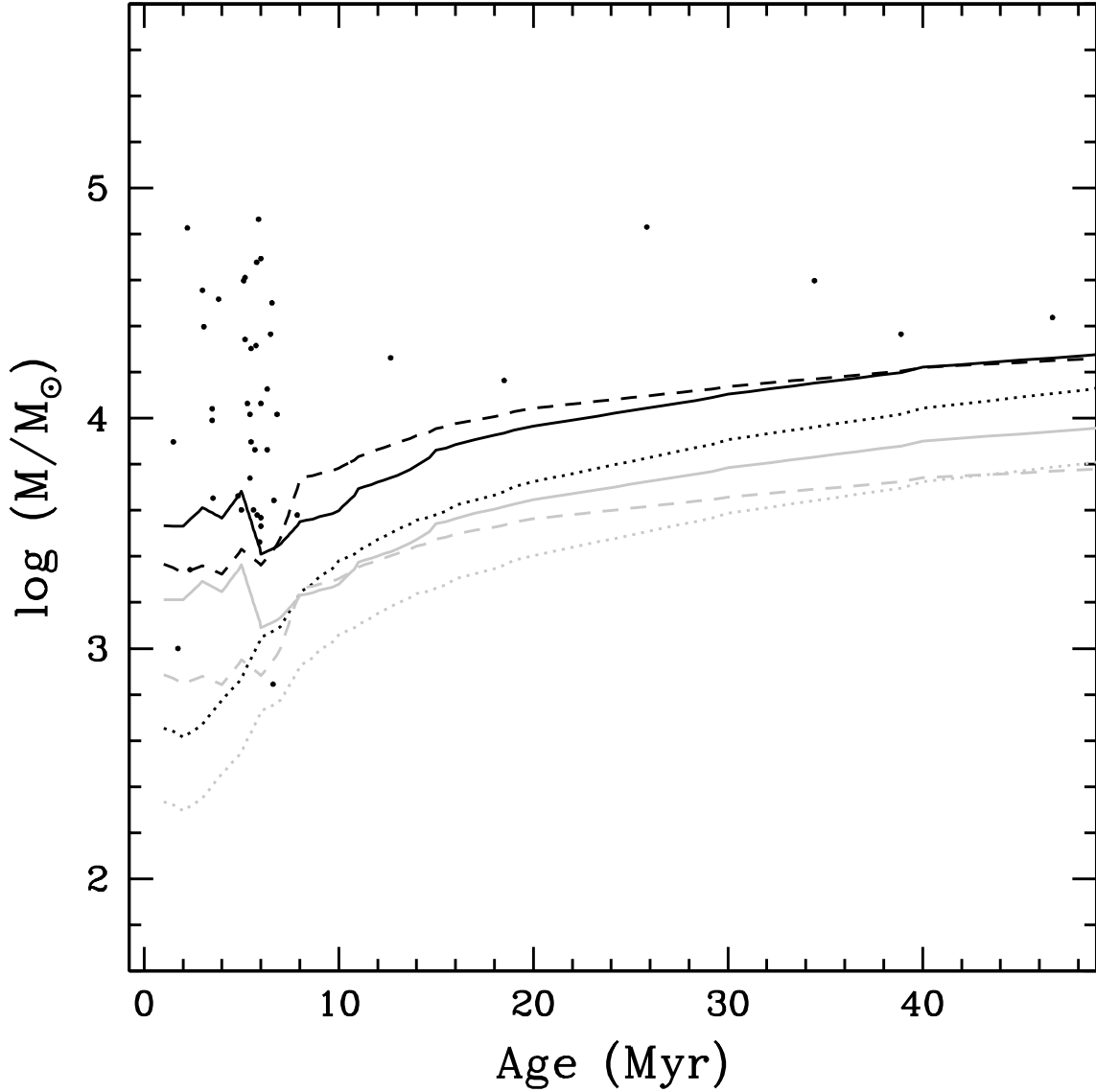


Fig. 12.— The relationship between mass and age for clusters in our sample. The curves represent the minimum observable mass as a function of age for the F300W (dotted lines), F547M (dashed lines) and F814W (solid lines) images. At each age, the minimum observable mass is taken from the faintest Starburst99 model point brighter than our 90% (black lines) or 50% (grey lines) completeness limits in each image.

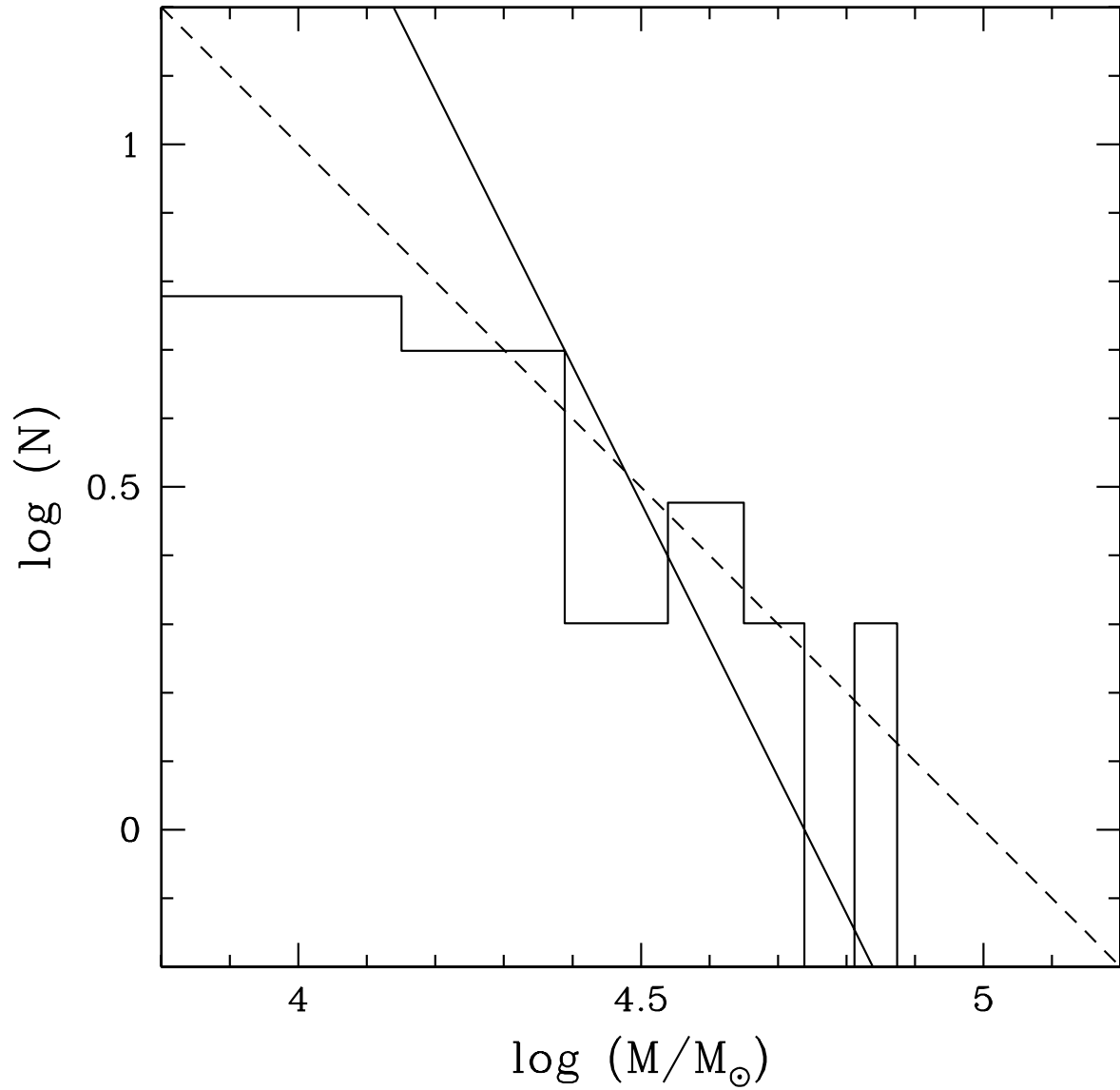


Fig. 13.— The distribution of masses for young (age < 10 Myr) clusters in our sample. The solid line represents a power law with  $\alpha = -2.0$ , which is similar to the mass function observed in major-merger starbursts. The dashed line represents a power law with  $\alpha = -1.0$ .